Hindawi
International Journal of Aerospace Engineering
Volume 2023, Article ID 7687760, 22 pages
https://doi.org/10.1155/2023/7687760

Research Article

Influence of Rotating Speeds and Thermodynamic Effects on LOX Turbopump Performance

Xuebing Bu[1], **Ping Fu**[2], **Hongchuan Cong**[1] and **Zhongguo Sun**[1]

[1]*Department of Fluid Machinery and Engineering, School of Energy and Power Engineering, Xi'an Jiaotong University, Xi'an 710049, China*
[2]*Xi'an Zhongke Aerospace Power Technology Co. Ltd., Xi'an 710100, China*

Correspondence should be addressed to Zhongguo Sun; sun.zg@xjtu.edu.cn

Received 12 December 2022; Revised 17 February 2023; Accepted 23 February 2023; Published 3 April 2023

Academic Editor: Qingfei Fu

As a key factor of a reusable turbopump, axial thrust directly determines the reliability of the bears and seals, especially considering the influence of rotational speeds and thermodynamic effects. In this study, numerical simulations and experimental tests were conducted to explore the impact of rotational speeds and the divergences of the turbopump performance with/without the thermodynamic effects. The experimental data obtained at 15000 r/min are in good agreement with the numerical results, illustrating the validity of the numerical model. The results show that the head deviations based on the affinity laws are relatively smaller, only 0.1% difference at normal condition, yet the efficiency increases from 72.5% to 73.8%, which need to be modified through the formula correction. Notably, the axial thrusts acting on impeller are significantly affected by the rotational speeds, and the values at rated flowrate decrease 17.6% after increasing the operating condition to rated speed. The affinity laws are not applicable for obtaining the turbopump axial thrusts under different speeds. Furthermore, due to the changes of the local physical properties, the values of head coefficient and efficiency decrease 2.8% and 1.3% at rated flowrate, respectively, when the thermodynamic effects of liquid oxygen are considered. Meanwhile, the relative variations of axial thrust are between 1.46% and 3.74% within the whole flow range. Finally, an in-depth analysis of the internal flow was conducted through the velocity field and vorticity method. In conclusion, both the rotational speeds and thermodynamic effects significantly affect the performance of a cryogenic turbopump, especially the axial thrust, and the unsteady results of the rotor-stator cavity leakage flow need to be analyzed in the future.

1. Introduction

The function of a turbopump, a main component of the liquid propellant rocket engine, is to pressurize the propellant to meet the engine system requirements [1]. Nontoxic and nonpolluting propellants, such as liquid oxygen (LOX), kerosene, and liquid hydrogen, have been widely applied, owing to the environmental protection and staff health [2, 3]. Moreover, a centrifugal pump is an energy conversion device that is widely used in the cryogenic refrigeration industry and petrochemical industry [4, 5]. A common feature of the above components is that the media pumped are all cryogenic media. As is well known, the physical properties of a cryogenic medium are closely related to the local temperature and pressure, which is the so-called thermodynamic effects. Additionally, the tendency of variable thrust and reusability of rocket engines has placed extremely stringent requirements on the development of turbopumps [6–8]. As an important factor, the axial thrust of a turbopump plays an important role and is affected by the physical properties of the cryogenic medium [9]. Owing to the adjustment of operating conditions, the flow rates and discharge pressures of the turbopump should be adaptively altered through the rotational speeds. Hence, the influence of the thermodynamic effects and rotational speeds needs in-depth study to ensure the turbopump performance and reliability.

Due to the urgent requirement for delivering cryogenic medium (such as LOX and LCH4) over a wide flow range, the pump performance under off-design condition has been

researched widely. Experimental test and numerical simulation are the two main methods that provide an in-depth understanding on this issue [10, 11]. Currently, due to the high cost of experimental test and improved accuracy of numerical simulation, the research strategy of preliminary simulation analysis and final experimental verification is generally adopted [12–14]. In terms of the operating conditions of centrifugal pumps, the working conditions of a turbopump can be realized by varying the rotational speeds or flow rates. Yang et al. [15] employed a typical electrical submersible pump to verify the similarity of the pump performance under different rotating speeds, and they found that the maximum efficiency of the model pump slightly improves after increasing the rotation speed. Xu et al. [16] and Han and Tan [17] investigated the influence of rotation speed on the pressure fluctuations. Additionally, Dodsworth and Groulx [18] studied the influence of motor speeds to obtain the performance curves of a tesla pump. Interestingly, Tsukamoto et al. [19] conducted experimental tests and theoretical analyses to study dynamic characteristics of a centrifugal pump with fluctuating rotational speeds. Based on their respective mechanical models, Vermunt et al. [20], Ogata et al. [21], and Zheng et al. [22] studied the characteristics of their research objects under variable rotating speeds, such as rotation stall, additives for drag reduction, and vibration behaviors. Owing to the potential energy savings, the implementation of variable-frequency drives in electric motors has also been evaluated [23–25]. Moreover, Tanaka and Tabaru [26] studied the transient behavior of a centrifugal pump during rapid start-up. Duplaa et al. [27–29] also revealed that the performance during the pump rapid start-up greatly deviates from that in quasi-steady condition, owing to the rotational speed acceleration and flow rate acceleration. In the above studies, centrifugal pumps or other hydraulic machineries were employed as research models, and the external characteristics were mainly focused on. However, the internal flow distributions under different operating speeds, especially the leakage flow in the rotor-stator cavity, are not studied enough.

Another key aspect of this paper is the influence of thermodynamic effects on the turbopump performance. Extensive related studies have also been conducted, mainly focusing on the differences of the inducer cavitation. Over the last 15 years, Japan Aerospace Exploration Agency (JAXA) has devoted significant efforts to comprehensively explore this issue, for enhancing the performance and reliability of the liquid hydrogen/oxygen turbopump applied to LE-7 rocket engine [30–36]. Watanabe et al. [30, 31] presented the heat transfer model to analyze the thermodynamic effects on cavitation instabilities using the singularity method. At almost the same time, Yoshida et al. [32–34] analyzed the thermodynamic effects on the cavitation performances and cavitation instabilities of a rocket engine inducer, to determine the evolution mechanism of subsynchronous rotating cavitation. To meet the requirements of liquid rocket engines, researchers are still comprehensively exploring the thermodynamic effects of cryogenic media [35–40]. In addition to the thermodynamic effects on cavitation, Li et al. [41] employed a liquid oxygen turbopump to investigate the thermodynamic effects on pressure fluctuations. During the exploitation of a new generation launch vehicle, detailed pressure distributions on the rear side of the impeller, which affect the axial thrust characteristics, were obtained via compressible simulation [42–44]. Recently, Bu et al. studied the thermodynamic effects of liquid oxygen on the flow distributions in the rotor-stator cavities of a cryogenic turbopump [45]. The current researches pay more attention to the influence of thermodynamic effects on the inducer cavitation; however, the influence of the cryogenic medium on the axial thrust needs to be further analyzed.

Previous studies have categorically studied the influence of rotating speeds and thermodynamic effects. However, the previous research mainly focuses on the external performance and vibration characteristics, the operating speeds are relatively lower, and the pressurized medium is mostly water or hydraulic oil. Meanwhile, the thermodynamic effects of cryogenic media mainly focus on the characteristics of cavitation, which mostly occurs in the inducer or volute throat. Few conclusions have been conducted on the impact of the characteristics of internal flow, especially in the rotor-stator cavities. In this paper, the influence of rotating speeds and thermodynamic effects was investigated to obtain the variations of an LOX turbopump performance, especially the leakage flow in the rotor-stator cavities. This paper is organized as follows. In Section 2, the test pump parameters and experimental setups are presented, including the basic information of the LOX turbopump and composition of the experimental system. In Section 3, numerical results and experimental data are presented and compared to validate the numerical model. In Section 4, the differences of the turbopump performance are discussed under considering the influence of rotation speeds and thermodynamic effects. In Section 5, the main conclusions are presented with the significances and limitations of this study.

2. Pump Geometry and Experimental Test Rig

2.1. Basic Parameters of Liquid Oxygen Turbopump. A turbopump is used as the pressurization pump in the propellant system of a rocket engine to transport the propellant (e.g., LOX and RP-1). The LOX turbopump employed is a centrifugal pump with a speed ratio of 32. The specific speed is defined as follows:

$$n_s = \frac{n\sqrt{Q_v}}{H^{0.75}}, \tag{1}$$

where n is the rotational speed, Q_v is the rated flow rate, and H is the normal head.

The LOX turbopump employed comprises a two-blade inducer and a twelve-blade impeller (half of the blades are splitter blades). The inducer and impeller are driven by a gas turbine, and the turbopump rated speed is 30,000 r/min. Same as the research model employed in reference [45], the main parameters of the turbopump are illustrated in Table 1.

Figure 1 shows the images of the inducer and impeller used herein. Note that this inducer has a sweptback leading

Table 1: Main design parameters of the LOX turbopump.

Design parameter	Symbol	Value	Unit
Rated head	H_d	1148	m
Rated flow rate	Q_v	0.036	m^3/s
Rated rotational speed	n_d	30000	r/min
Efficiency	η	72.4	%
Specific speed	n_s	32	—
Inlet diameter of impeller	D_1	64	mm
Outlet diameter of impeller	D_2	112	mm
Outlet width of impeller	b_2	9	mm
Blade number of impeller	Z_{im}	6 + 6	—
Blade number of inducer	Z_{in}	2	—

edge, which is optimal for suppressing the cavitation surge. The impeller has additional six splitter blades to weaken the effect of the "jet-wake" flow and enhances the impeller capacity. Moreover, the materials of the inducer and impeller have identical thermal expansion coefficients; hence, the ratio of the radial tip clearance to the blade height is maintained in a liquid oxygen environment.

Additionally, the media pressurized by the turbopump are water and liquid oxygen, and they are applied for the subsequent experimental verification and numerical simulation.

2.2. Tested Pumping System. Water tests were conducted to verify the overall performance of the turbopump. The test rig was constructed at Xi'an Jiaotong University, and it is schematically depicted in Figure 2. The closed-loop facility comprises a water tank, rotating parts, control valves, suction pipe, and discharge pipe; meanwhile, the temperature transducer, pressure transducer, turbine flowmeter, and the gear rotating speed transducer are equipped to measure the experimental parameters. Filtered water is stored in a 5.6 m^3 stainless tank, and the pressure of the water tank is controlled through either a compressor or vacuum pump. Rotating parts include the test pump, speed-up gearbox, torque meter, and driving motor. The rated speed and power of the driving motor are 2900 r/min and 300 kW, respectively. The maximum operating speed and maximum power of the gearbox are 17,000 r/min and 350 kW, separately. The rotational speed is controlled within 0.02% using a variable frequency drive. The flow rate of the test pump is precisely controlled by the pneumatic regulating valves.

To prevent the potential risk from excess materials, water from the tank flows through the filter firstly. A pressure transducer and a temperature transducer are installed at more than 10 pipe diameters upstream of the test pump, and the torques and rotational speeds are measured using a compound torque meter. In this paper, the test pump rotational speed was fixed as 15000 ± 30 r/min. The mean flow rate is measured downstream of the test pump through an electromagnetic flow meter, and it is regulated by precisely controlling the valve opening. The uncertainty of each parameter with 95% confidence interval is as follows: ±0.42% of the head and ±0.16% of the mass flow rate.

Figure 3 shows the test section of the experimental system, which mainly consists of a test pump, test bracket, speed transducer, and the gearbox. The inlet and outlet pipes of the test pump are connected to the straight pipe of the experimental system through the flanges, and a customized flange is rigidly fastened between the test pump and the bracket. Owing to the high operating speeds, high-precision splines are chosen to transmit the rotational speed and torque. All controlled variables and acquisition parameters are measured using the measurement and control system.

The experimental tests are conducted in noncavitation conditions. Before each test, the suction pressure was maintained to be higher than the critical cavitation pressure to avoid the impact of cavitation.

3. Numerical Strategy and Test Verification

3.1. Computational Domain. The entire computational domain is exhibited in Figure 4, including inlet pipe, pump casing, inducer, impeller, volute, and outlet pipe. To obtain the realistic performance of the turbopump, both the shroud cavity and rear cavity are considered in the numerical simulation. Furthermore, the inlet and outlet pipes are extended to eliminate the interference of the physical model on the numerical calculations. To improve the numerical convergence, the inlet pipe is extended by eight times the inlet pipe diameter, and the outlet pipe is lengthened by ten times the outlet pipe diameter.

3.2. Grid Independence Verification. In this study, the grids were generated via ICEM CFD. Consistent with the grid strategy in reference [45], a hexahedron structure grid with small truncation error and good convergence was selected to discretize all computational domains to ensure the accuracy of the numerical simulation, as shown in Figure 5. The mesh of the narrow gaps was refined, such as the clearance in the shroud cavity and rear cavity, especially the annular gap between the rotating impeller and stationary casing [46].

Firstly, a brief overview of the numerical setup is presented. Reynolds averaged Naiver-Stokes (RANS) method was employed to simulate the internal flow of the LOX turbopump. The finite volume method was used to solve the system of equations in commercial software ANSYS-CFX. Since it is extensively benchmarked for turbomachines, the shear stress transport (SST) turbulence model proposed by Menter et al. [47] with automatic wall-treatment was employed to compile the governing equations, similar to Tanaka et al. [13] and Chabannes et al. [48]. A high-resolution scheme was utilized for the advection scheme to achieve robust and accurate solutions. The value of residual target was set as 10^{-4}. As the boundary of the CFD simulations, the mass flow rate and the turbulence intensity of 0.05 (representing a medium turbulence level) were specified at the outlet of the computational domain. At the inlet of draft tube, a static pressure was considered for more robust calculations.

(a) Inducer (b) Impeller

Figure 1: Inducer and impeller after hydraulic tests.

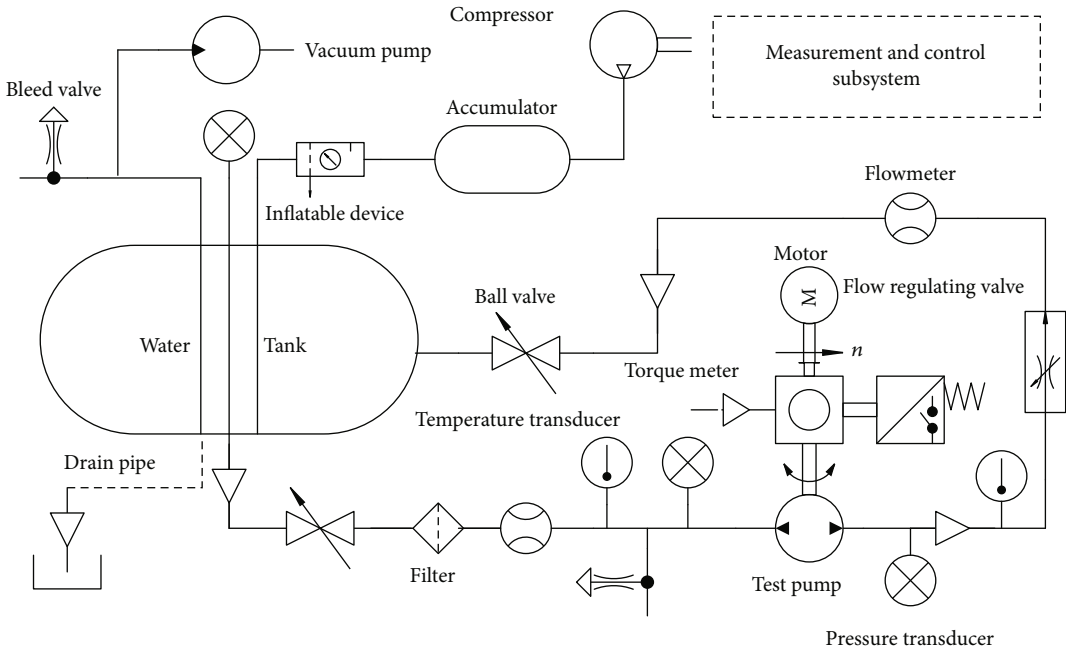

Figure 2: Schematic of the experimental test rig.

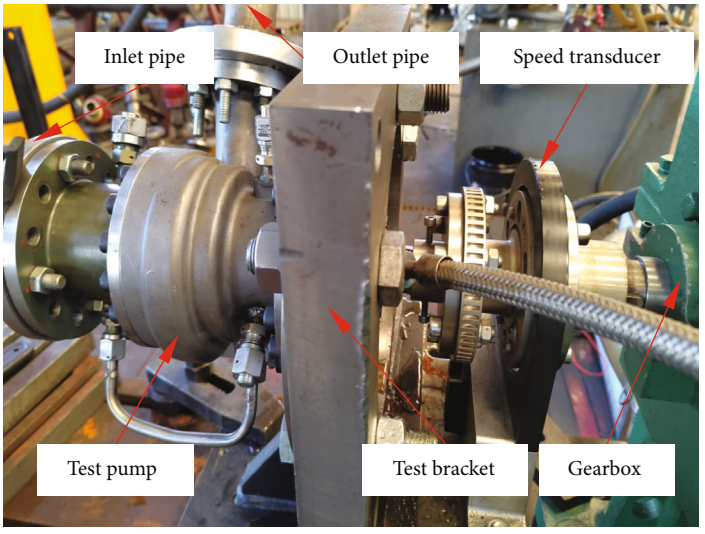

Figure 3: Test facility at Xi'an Jiaotong University.

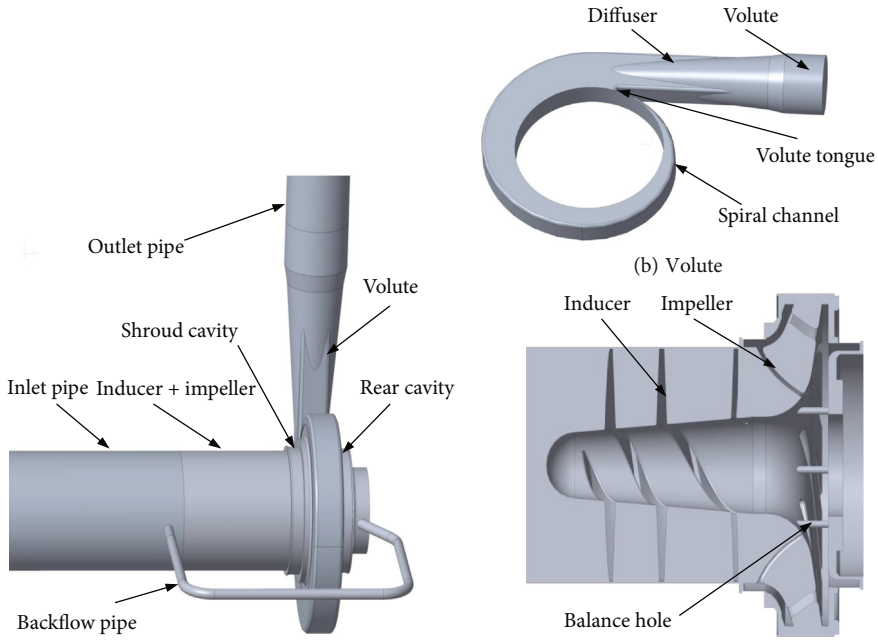

Figure 4: Fluid domains and 3D model of the turbopump.

The flow coefficient ϕ, head coefficient ψ, and efficiency η were used to characterize the performance of the LOX turbopump as the nondimensional parameters, and they are defined as follows [49]:

$$\text{Flow coefficient, } \phi = \frac{Q}{nD_2^3}, \tag{2}$$

$$\text{Head coefficient, } \psi = \frac{\Delta P}{\rho D_2^2 n^2}, \tag{3}$$

$$\text{Efficiency, } \eta = \frac{\rho g H Q_V}{\sum M_i \omega} = \frac{\Delta P Q_V}{\sum M_i \omega}, \tag{4}$$

where ρ is the fluid density and ΔP is the total differential pressure between the inlet and outlet of turbopump.

In Table 2, taking water as the medium, five sets of grids were tested (cases A~E) at rated speed ($n = 30000$ r/min), and variations of the calculated head coefficient ψ and efficiency η are given. To be clear, the value of the flow coefficient ϕ is 1.74×10^{-3} at rated condition. Comparison of the numerical results obtained from cases D and E clearly shows that the number of grid nodes has little impact on the numerical predictions, which means that the number of grids is sufficient. Considering the computational cost and numerical accuracy, case D is selected for the subsequent numerical calculations. In addition, the values of y^+ distributed on the impeller are less than 50, which can completely satisfy the requirement of the turbulence model.

3.3. Experimental Verification. Figure 6 compares the performance curve of the LOX turbopump obtained via numerical simulation with the experimental results. For the LOX turbopump, the real working conditions of cryogenic liquid at 90 K are difficult to achieve, and the experimental cost is too expensive. Hence, water at 298 K was chosen to conduct the experiment and verify the turbopump simulation. To obtain accurate experimental data and reduce the measurement errors, the experimental tests were conducted thrice at 15000 r/min. The results show that the values of the head coefficient and efficiency obtained by the numerical simulation well match the experimental data. The relative errors between the numerical and experimental results are less than 5% over the test flow range.

In Figure 6, a comparison was performance between the performance curves of the numerical simulation and experimental data under different flow coefficients. Based on numerical simulation results, the head coefficient predicted via numerical simulation is 0.56% higher than the experimental value, and the efficiency is 1.68% higher than the experimental value at the rated condition. Furthermore, the differences between the numerical and experimental values increase with the decrease of flow rate. The divergences between the simulated and experimental values are caused by the simplification of the real state of the tested product and the accuracy of the numerical model. As shown in Figure 6, the variations between the numerical results and experimental data are within a certain range. It is demonstrated that the simulated model presented herein can be applied to conduct a numerical investigation.

4. Results and Discussion

To investigate the influence of the rotating speeds and the thermodynamic effects on the performance of the turbopump, steady simulation with validated numerical schemes was conducted.

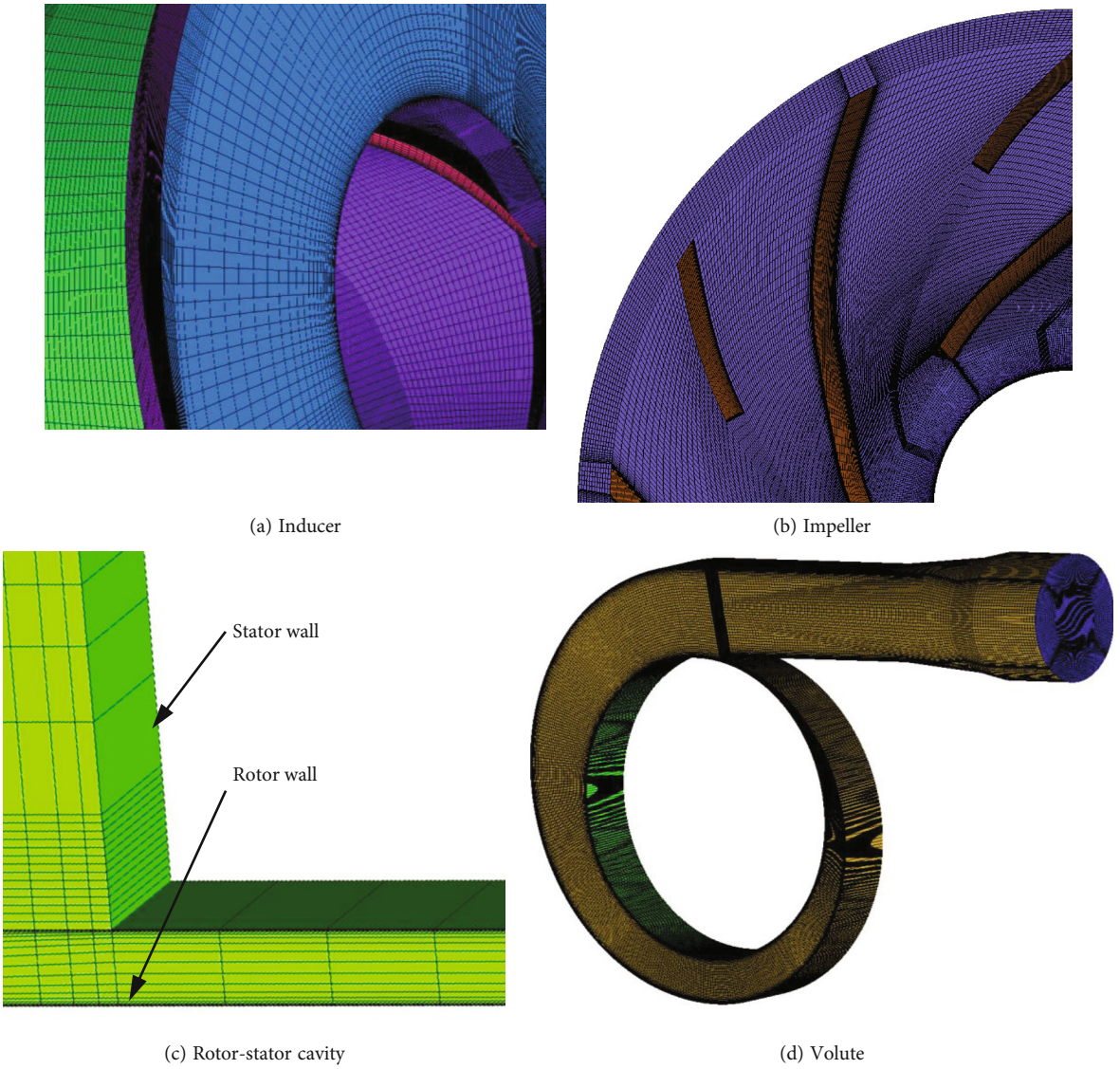

(a) Inducer (b) Impeller

(c) Rotor-stator cavity (d) Volute

Figure 5: Mesh arrangement of the turbopump.

4.1. Influence of Variable Rotating Speeds. Notably, the affinity laws of a centrifugal pump relate the variations in volume flow, head, and power. These laws are used to obtain the performance curves of the pump at different angular velocities or with different impeller diameters [9]. The corresponding equations of the volumetric capacity Q, head H, and power P are as follows:

$$\frac{Q_2}{Q_1} = \left(\frac{n_2}{n_1}\right)\left(\frac{D_2}{D_1}\right)^3, \tag{5}$$

$$\frac{H_2}{H_1} = \left(\frac{n_2}{n_1}\right)^2\left(\frac{D_2}{D_1}\right)^2, \tag{6}$$

$$\frac{P_2}{P_1} = \left(\frac{n_2}{n_1}\right)^3\left(\frac{D_2}{D_1}\right)^5. \tag{7}$$

Here, D represents the diameter of the impeller.

Keeping the medium as water and the structural size of the turbopump unchanged, the performance curves of the turbopump under $0.5n_d$ and n_d are compared in Figure 7.

Figure 7 clearly shows that the rotation speeds have certain influence on the turbopump performance, especially the efficiencies. When the rotational speed of the turbopump increases from $0.5n_d$ to n_d, the efficiencies via numerical simulated change from 72.5% to 73.8% at rated flow, which is very sensitive and essential for adjusting the parameters of the engine system. As the flow rates deviate from the normal condition, the divergences of the total efficiency decrease at the off-design conditions. Contrary to the evolution tendency of the efficiency, the values of the head coefficient ψ exhibit a completely different feature with varying rotation speeds. When the rotational speed increases from $0.5n_d$ to rated speed, the head coefficients obtained at rated flow are 1.451×10^{-3} and 1.452×10^{-3}, respectively, and the relative

Table 2: Grid independence study results.

Case	Mesh nodes (million)	Head coefficient (ψ)	Relative change of head (%)	Efficiency η (%)	Relative change of efficiency (%)
Case A	7.26	1.438×10^{-3}	-1.10	73.35	-0.65
Case B	9.79	1.442×10^{-3}	-0.83	73.41	-0.57
Case C	12.24	1.447×10^{-3}	-0.48	73.72	-0.15
Case D	14.65	1.452×10^{-3}	-0.14	73.84	0.01
Case E	17.26	1.454×10^{-3}	0	73.83	—

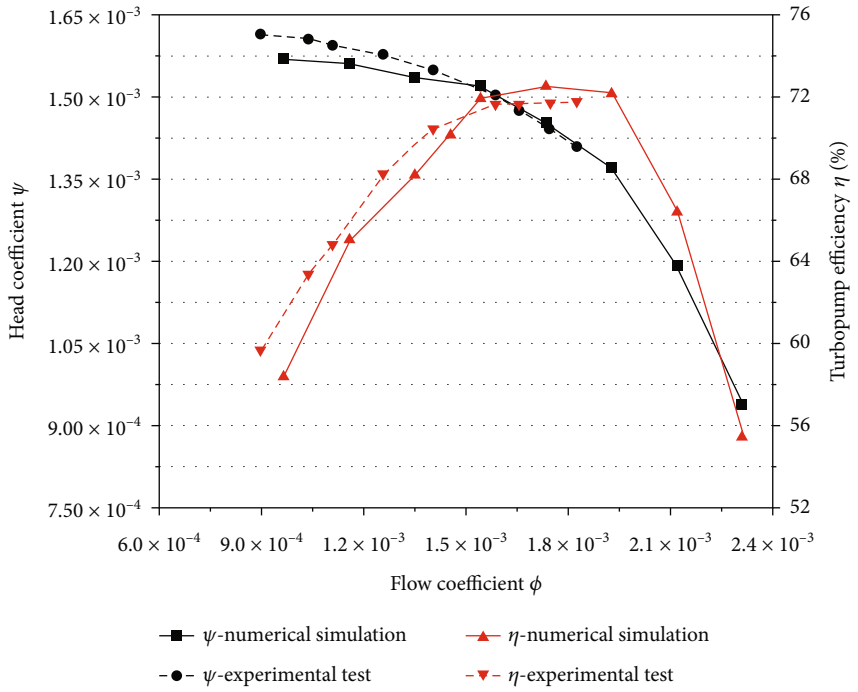

Figure 6: Comparison of the performance obtained by experimental and numerical results.

change amplitude based on the rated speed is 0.07%, which is small enough to be ignored. Similarly, the head coefficients under off-design conditions are also analyzed, and the head coefficients are 2.31% and 4.76% lower at flow coefficient $\phi = 5.79 \times 10^{-4}$ and $\phi = 2.51 \times 10^{-3}$, separately, when the turbopump speed increases from $0.5n_d$ to rated speed. In comparison of the head coefficients and efficiencies obtained under variable rotational speeds, it is clear that the affinity laws of a centrifugal pump relating the variations of the head and efficiency are more effective with minor corrections, and the characteristics of the head coefficient and efficiency are different under different flow rates.

The turbopump internal flow is extremely complex. To further analyze the performance characteristics of the turbopump, the influence of rotational speeds on the turbopump volumetric efficiency is studied, as shown in Figure 8. The volumetric efficiencies in Figure 8 are defined as the ratio between the leakage flow through the rotor-stator cavity and the volume flow delivered by impeller. Nomenclatures η_{Vs} and η_{Vh} in the figure represent the volumetric efficiency of the shroud cavity and the rear cavity, respectively.

As shown in Figure 8, the deviations of the volumetric efficiency increase with the decrease of flow rate, when the turbopump speeds increase from $0.5n_d$ to rated condition. Consistent with the change trend of total volumetric efficiency, whether the rotor-stator cavity is a shroud cavity or rear cavity, the volumetric efficiencies synchronously decrease with the flow mate decreasing. However, after considering the influence of rotational speeds, the volumetric efficiencies of the shroud and rear cavities exhibit different variation trend, owing to the influence of the cavity structures. In the shroud cavity, as the rotational speed increases from $0.5n_d$ to n_d, the volumetric efficiencies change from 93.84% to 93.66% at rated flow, and the maximum deviation is 0.82% at $\phi = 5.79 \times 10^{-4}$. In the rear cavity, the volumetric efficiencies change slightly from 96.75% to 96.76% at rated flow. Generally, the rotational speed has a slight influence on the volumetric efficiency. Since the volumetric efficiencies of the turbopump change little, the efficiency differences are mainly caused by the hydraulic efficiency variations after the turbopump speed changes. According to the analysis of the turbopump efficiency, it was

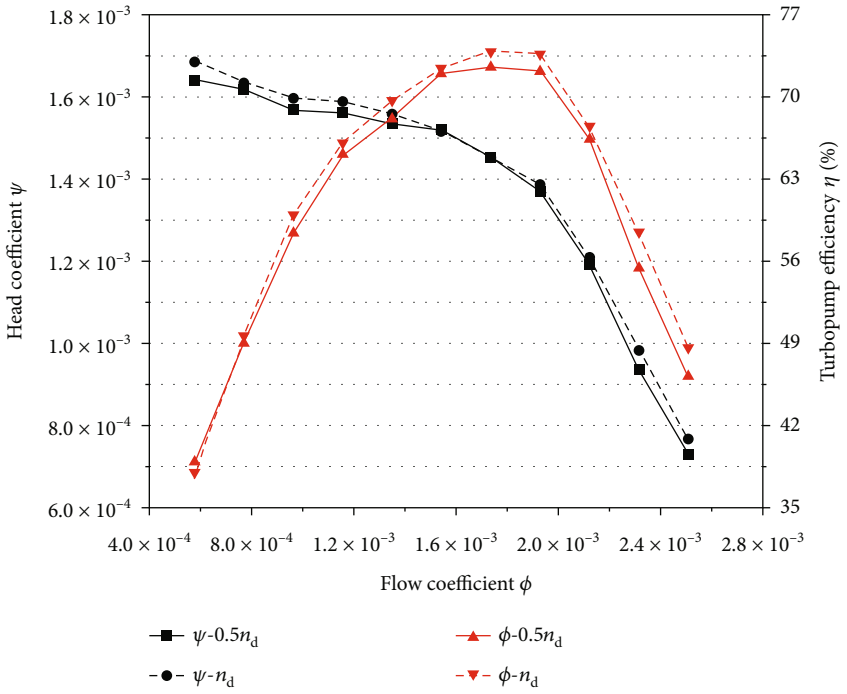

Figure 7: Comparison of the performance under different rotational speeds.

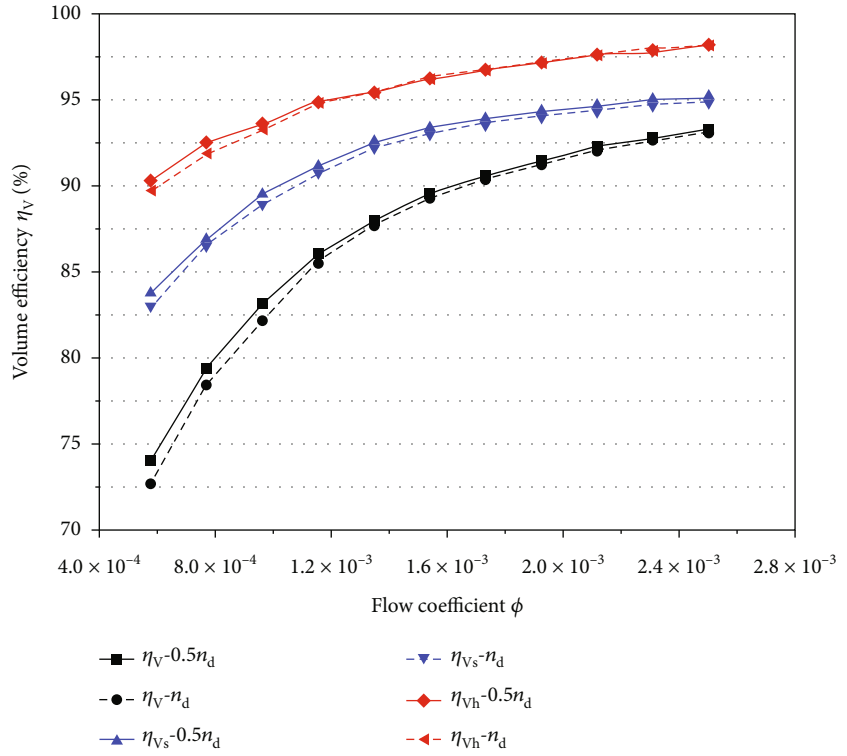

Figure 8: Comparison of the volumetric efficiency under different rotational speeds.

speculated that the changes of Reynolds number cause the variations of the turbopump hydraulic loss, resulting in the deviations of the hydraulic efficiency.

As mentioned above, the axial thrust of impeller is a key factor that decides the turbopump reliability when the thrust of the rocket engine is required to adjust. To analyze the impact of rotational speeds on the axial thrust, the axial thrust coefficient is introduced and defined as follows [50]:

$$C_F = \frac{T_p}{0.5\pi r_2^2 \rho u_2^2} = \int_{r_1}^{r_2} \frac{4p(r)rdr}{\rho\omega^2 r_2^4}. \quad (8)$$

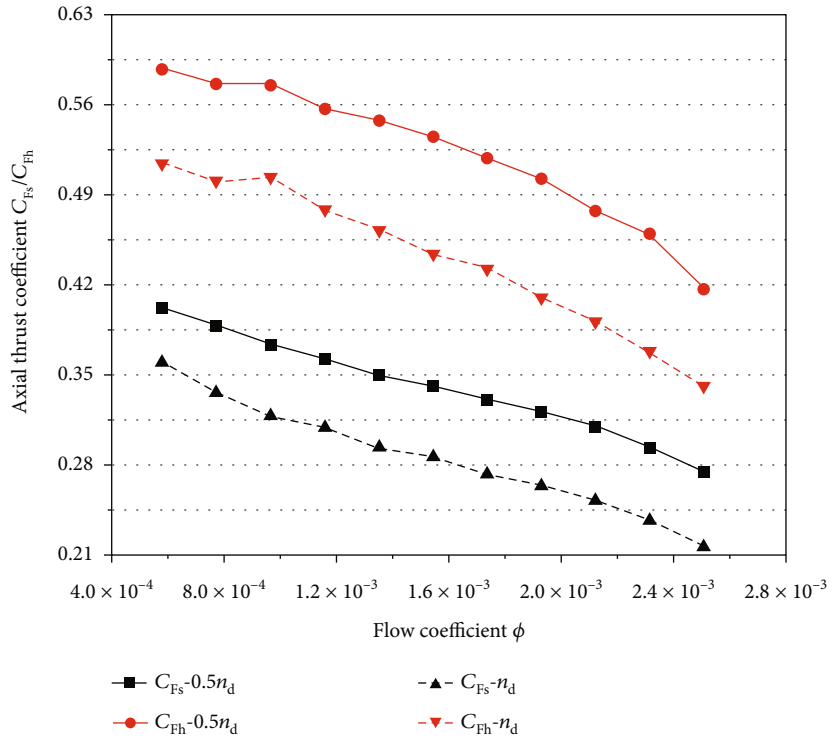

(a) Axial thrust coefficient C_{Fs} and C_{Fh}

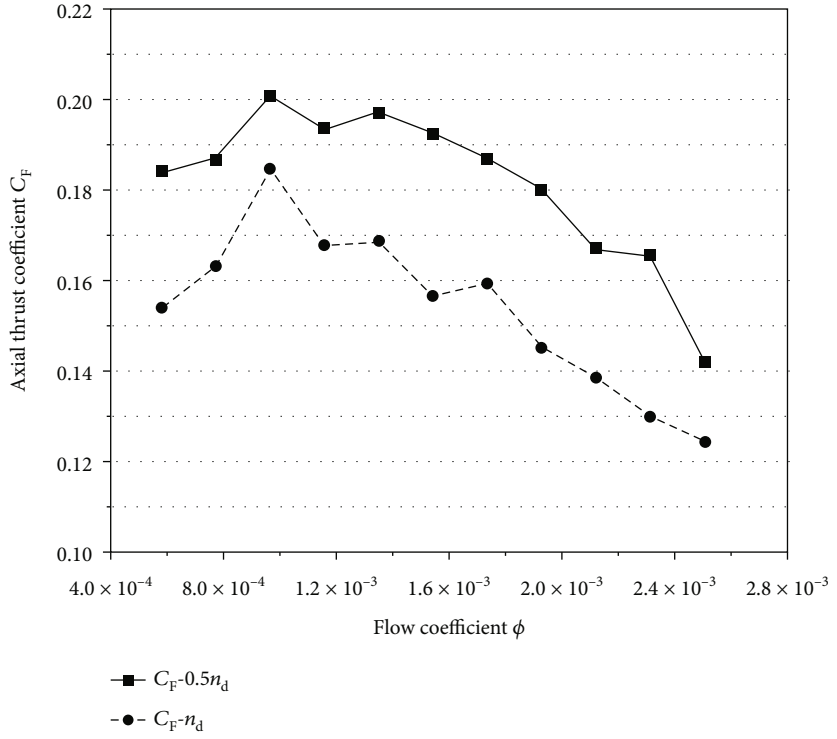

(b) Axial thrust coefficient C_F

FIGURE 9: Comparison of the axial thrusts under different rotational speeds.

The axial thrusts acting on the impeller in the above numerical conditions were calculated, and the values of both the impeller shroud and hub were analyzed, as shown in Figure 9. It should be noted that C_{Fs} and C_{Fh} represent the axial force acting on the impeller shroud and the impeller hub, respectively.

With distinct difference from the characteristics of head and volumetric efficiency in Figures 7 and 8, the axial thrusts

acting on the impeller do not conform to the affinity laws. For both the impeller shroud and the impeller hub, the axial thrust coefficients C_{Fs} and C_{Fh} monotonically increase with the decreasing flow at the same rotational speed. Moreover, keeping the flow coefficients constant, the axial thrust coefficients C_{Fs} and C_{Fh} increase with the decreasing rotational speed. As the turbopump speed increases from $0.5n_d$ to n_d, the axial thrust coefficient C_{Fs} decreases from 0.332 to 0.274 at rated flow, and C_{Fh} decreases from 0.519 to 0.433 under the same condition. Based on the axial thrusts obtained at rated speed, the relative changes of the axial thrust acting on the impeller shroud and the impeller hub are 21.2% and 19.9%, respectively. At lower rotational speed, when the flow coefficient ϕ decreases from 2.51×10^{-3} to 5.79×10^{-4}, the axial thrust coefficient C_{Fs} increases from 0.275 to 0.403, and these values acting on the impeller hub increase from 0.417 to 0.587, respectively. At rated speed, when the flow coefficient ϕ decreases from 2.51×10^{-3} to 5.79×10^{-4}, the axial thrust coefficient C_{Fs} increases from 0.217 to 0.361, and C_{Fh} increases from 0.342 to 0.515, respectively. The above results show that the rotational speed significantly affects the axial thrust. Owing to the divergences between C_{Fs} and C_{Fh}, we can find that the structures of the rotor-stator cavities also influence the distributions of the axial thrust. According to the relative magnitude of the axial thrust coefficient, regardless of whether the turbopump operating condition is at rated flow or off-design condition, the axial thrust coefficients do not obey the affinity laws of centrifugal pumps.

Figure 9(b) shows the changes of the total axial thrust coefficient C_F under different rotational speeds. Owing to the higher impeller outlet pressure at the smaller flow rate, the axial thrust coefficient C_F in general increases as the flow coefficient decreases, no matter how the rotational speed changes. When the turbopump speed decreases, the axial thrust coefficient C_F at normal flow increases from 0.159 to 0.187, and the relative amplitude is 17.6%. The results reveal that there are large deviations when the affinity laws are used to recklessly convert the axial thrust.

As described in the previous study, the axial thrust acting on the impeller is obtained by integrating the static pressure along the radial direction [51], and the static pressure is achieved by the following formula:

$$p(r) = p_2 - \rho\omega^2 \int_r^{r_2} k^2(r) r dr, \tag{9}$$

where k is the fluid rotation ratio [51] and is solved by

$$\frac{dk}{dx} = 0.07875 \frac{\pi\omega x^{8/5}}{Q_{cq}\,\mathrm{Re}_u^{1/5}} r_2^3 \left[\left(\frac{1-k_0}{k_0} k \right)^{7/4} - (1-k)^{7/4} \right] - 2\frac{k}{x}, \tag{10}$$

where $x = r/r_2$ is the nondimensional radius, Q_{cq} is the volumetric leakage flow, and $\mathrm{Re}_u = \omega r_2^2/\nu$ is the rotational Reynolds number.

As can be seen from Equation (10), keeping the turbopump geometry unchanged, there is a direct between the fluid rotational ratio k to angular velocity ω, the leakage flow Q_{cq}, and the rotational Reynolds number Re_u. Owing to the volume efficiency under different flow rates in Figure 8, we can find that the coefficient ω/Q_{cq} is approximately constant at each speed. Hence, it is obvious that the changes of the fluid rotational ratio k are caused by the rotational Reynolds number Re_u, which means that the differences of the axial force coefficient C_F in Figure 9 are mainly affected by the turbopump speed n.

4.2. Influence of the Thermodynamic Effects. Selecting water as the medium and without considering thermodynamic effects, the performance under variable rotational speeds was compared; the results indicate that the rotational speeds have an obvious impact on the axial thrusts. Furthermore, owing to the wide application of liquid oxygen in liquid propellant rocket engines, liquid oxygen was selected as the working medium to analyze the influence of the thermodynamic effects. Furthermore, the characteristics of the thermodynamic effects of liquid oxygen and the changes of the rotational speeds on the turbopump performance are discussed.

In this section, the influence of the thermodynamic effects at a constant rotational speed was studied. In the calculation, the total energy equation considering the viscosity effect and rotation energy was added to obtain the internal flow field, which is applicable to the temperature field calculation of turbopumps and other rotating machinery [41]. To analyze the influence of thermodynamic effects, physical parameters such as density, specific heat capacity, thermal conductivity, and dynamic viscosity that vary with temperature are fitted as functions and written into commercial software ANSYS CFX using CEL language. It should be noted that the saturation thermodynamic properties of liquid oxygen are used here to fit the physical property formulas, due to the sensitivity of physical properties to the local temperature, compared with the pressure. Equations (11)–(14) provide the fitting formulas under liquid oxygen temperatures of 75-120 K [52].

$$\rho = 1430.1327 - 1.3895 \cdot T - 0.02005 \cdot T^2, \tag{11}$$

$$c_p = 0.73639 + 0.03652 \cdot T - 4.82515 \times 10^{-4} \cdot T^2 + 2.17343 \times 10^{-6} \cdot T^3, \tag{12}$$

$$\lambda \times 10^3 = 273.9234 - 1.2605 \cdot T - 0.00106 \cdot T^2, \tag{13}$$

$$\mu \times 10^6 = 3320.1395 - 79.7493 \cdot T + 0.67888 \cdot T^2 - 0.00198 \cdot T^3. \tag{14}$$

Here, T represents the local temperature. To ensure that the above equations can accurately reflect the changes of the physical properties of liquid oxygen with temperature rise, the values of the coefficient of determination (R^2) were calculated, and the corresponding values of the fitting formulas are all greater than 0.95.

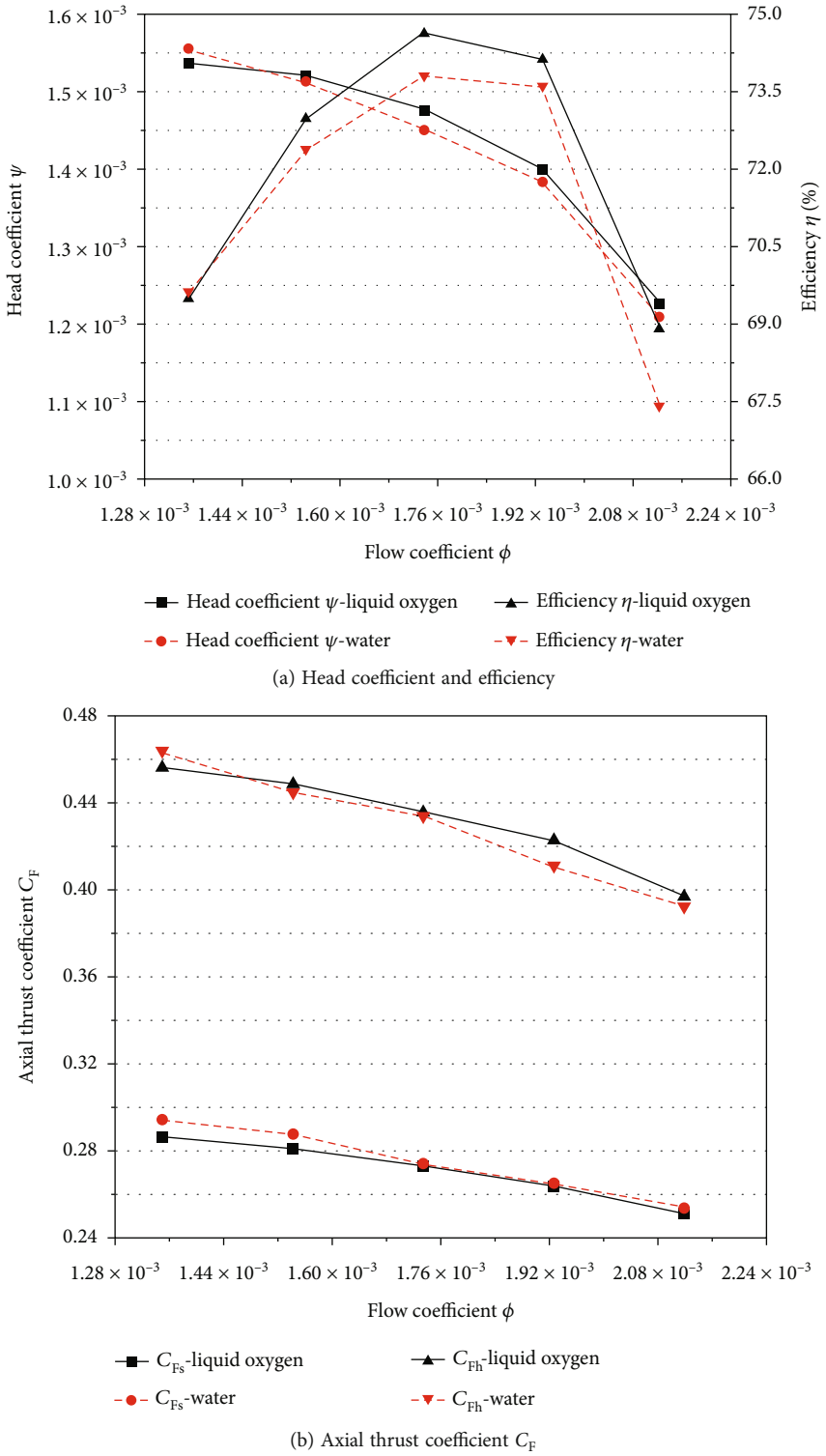

FIGURE 10: Comparison of the performance under different media.

Firstly, the physical properties of liquid oxygen were kept constant, and the total energy equation was added into the code. Figure 10 displays the performance obtained at rated speed, which is compared with the numerical results using water as the medium. Based on the performance characteristics of the centrifugal pump, the outlet boundary condition of the turbopump is determined to ensure consistent volume flow, and the initial temperature of the numerical simulation is 90 K.

As shown in Figure 10, due to the differences of physical properties between liquid oxygen and water, the head coefficients and efficiencies of the turbopump exhibit obvious divergences among the simulated flow coefficients. In

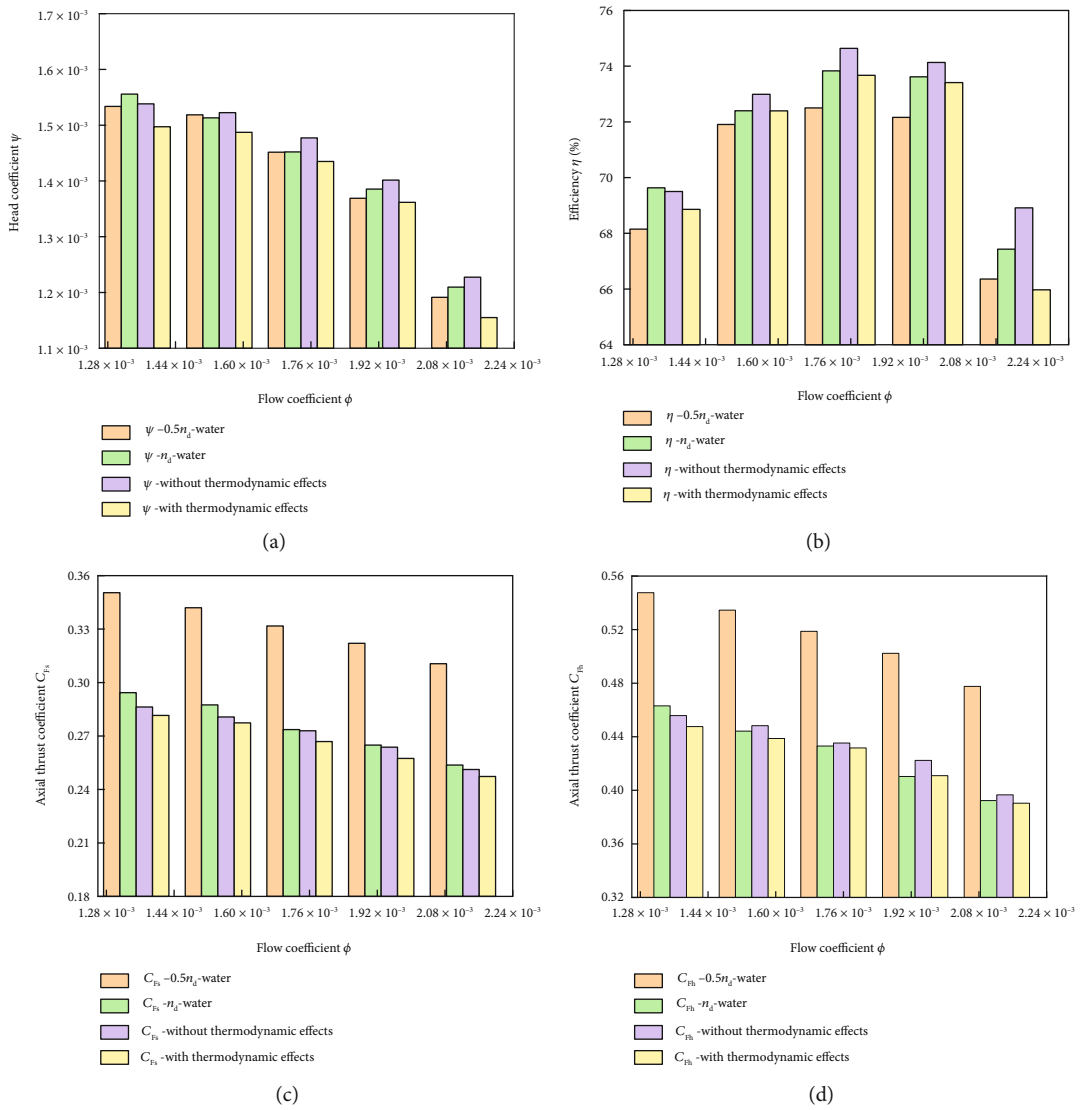

FIGURE 11: Comparison of the performance with and without thermodynamic effects. (a) Head coefficient, (b) efficiency, (c) axial thrust coefficient C_{Fs}, and (d) axial thrust coefficient C_{Fh}.

Figure 10(a), the head coefficients vary from 1.45×10^{-3} to 1.48×10^{-3} at rated flow, and the turbopump efficiencies increase from 73.83% to 74.64%. When the medium is changed from water to liquid oxygen, the dynamic viscosity significantly reduces, thus inhibiting the turbulent dissipation; consequently, both the head coefficients and efficiencies improve across the flow range, except for the smallest flow rate. The characteristics of head and efficiency in Figure 10(b) significantly differ from those in Figure 10(a); the changes of the axial thrust coefficient do not exhibit any obvious trend, regardless of the cavity structure. Based on the results of water, the maximum relative change of the axial thrust coefficient C_{Fs} is 2.74% at $\phi = 1.35 \times 10^{-3}$, and that applied to the impeller hub is 2.94% at $\phi = 1.93 \times 10^{-3}$. Interestingly, the axial thrusts acting on the impeller hub exhibit the same variation with the head coefficient. This phenomenon can be explained by the higher outlet pressure of the centrifugal impeller and the higher pressure distribution in the rotor-stator cavity, which results in higher axial thrusts. However, the axial thrusts acting on the impeller shroud exhibit totally different tendency, and the mechanism analysis of the axial thrusts acting on the impeller hub is not applicable here. Clearly, the media pressurized by the turbopump have a certain impact on the external characteristics and internal flow field, and owing to the divergences between the shroud cavity and rear cavity, the axial thrust coefficients exhibit some special features.

Based on the above numerical simulations of turbopump, the influence of thermodynamic effects was considered, which was realized by inserting Equation (11)–Equation (14) into the commercial code. Figure 11 shows the turbopump performance at different flow coefficients, with and without the influence of thermodynamic effects. In order to better analyze the influence of rotational speeds and thermodynamic effects on the turbopump performance, the simulated values in Figure 9 were drawn and compared again.

When considering the influence of the thermodynamic effects, the density of liquid oxygen depends on the medium temperature; thus, to unify the benchmark for comparison, the physical parameters at the inlet boundary of the turbopump were selected to conduct a dimensionless analysis.

As shown in Figure 11, quite distinct from the influence of the rotational speeds, the head coefficient and efficiencies of the turbopump significantly change in all calculated flow conditions, and the axial thrusts acting on impeller decrease by varying degrees. After considering the thermodynamic effects, the head coefficient decreases from 1.477×10^{-3} to 1.435×10^{-3}, and the efficiency of the turbopump decreases from 74.64% to 73.67% at rated condition. Similarly, the axial thrust coefficient C_{Fs} (shroud cavity) decreases from 0.273 to 0.267, and the axial thrust coefficient C_{Fh} (rear cavity) decreases from 0.436 to 0.431 at the same working point. In Figure 11(a), the head coefficients and efficiencies reduce under off-design conditions. The maximum relative variation of the head coefficient is 5.9% at $\phi = 2.12 \times 10^{-3}$, and that of efficiency is 4.3% under the same flow coefficient. The energy generated by the turbulent dissipation causes the temperature of the medium to increase, and subsequently, the density of the medium and the outlet pressure of turbopump are decreased. Combined with the research in Section 4.1, the performance curves of the turbopump obtained via a hydraulic test cannot be directly converted to obtain the performance data under a real medium; the rotational speeds and thermodynamic effects need to be considered to obtain accurate results, and the characteristics of their influence on turbopump performance are completely different. In Figure 11(b), due to the increase of temperature in the rotor-stator cavities, the density of liquid oxygen decreases, which causes the decrease of axial thrust coefficient obtained by the pressure integration in varying magnitudes. The axial thrusts exhibit maximum relative variation on both impeller shroud and impeller hub at $\phi = 1.93 \times 10^{-3}$. Moreover, the deviation of 2.4% and 2.8% can result in large absolute values when the axial thrust is obtained exactly, especially in the turbopump of high-thrust engine. Consistent with the head coefficient variation, to obtain sufficiently high-precision characteristics of the LOX turbopump, the thermodynamic effects need to be considered.

4.3. Comparison of Pressure within the Impeller. As is well known, the external performance and axial thrust are closely related to the pressure field distribution. Therefore, to further analyze the internal mechanism of rotational speeds and thermodynamic effects on the turbopump performance, a comparative study was conducted on the pressure field of the turbopump. Here, a nondimensional pressure is defined as a pressure coefficient [53].

$$C_p = \frac{p_l - p_i}{0.5\rho u_2^2} = \frac{p_l - p_i}{0.5\rho((\pi n D_2)/60)^2}. \quad (15)$$

Here, C_p is the pressure coefficient, p_l is the local pressure, p_i is the inlet pressure of turbopump, and u_2 is the circumferential speed of the impeller at the trailing edge.

To analyze the influence of the rotational speeds, Figure 12 shows the distributions of the static pressure coefficient in the rotation domain of turbopump under different flow coefficients, and the pressurized medium is water.

As shown in Figure 12, the pressure distributions in the impeller and rotor-stator cavities exhibits similar trends under the same flow coefficients, regardless of the variations of the rotational speed. However, owing to the influence of rotational speeds, the obvious contrast of the pressure coefficient can be discovered in the area around the impeller entrance, as indicated in Figure 12 using series numbers 1-4. Consistent with previous research results of centrifugal pumps, due to the rotation of impeller and the energy conversion in the volute, the pressure coefficient C_p increases from the leading edge of the impeller to the spiral channel of the volute, and the specific value decreases with increasing flow coefficient ϕ at the same location. Figures 12(b) and 12(e) display the distribution of the pressure coefficient at $\phi = 1.74 \times 10^{-3}$, with rotational speeds of $0.5n_d$ and n_d, respectively. The pressure coefficient C_p in the main flow channel, comprising the impeller and volute, is almost identical in any fluid domain, which can be verified through the head coefficient shown in Figure 8. Further comparison at the low flow coefficient of $\phi = 1.35 \times 10^{-3}$, similar to the rated condition, shows that the head coefficient exhibits the same characteristics, as shown by the polylines in Figures 12(a) and 12(d). As shown in Figures 12(c) and 12(f), after the flow coefficient is increased to $\phi = 2.12 \times 10^{-3}$, the rotational speeds of the turbopump have obvious effect on the pressure distribution in the main flow at the impeller eye.

Note that the pressure coefficient varies radially and has the same value in the axial direction in rotor-stator cavities, just the divergences of the radial location, which is convenient for correcting the one-dimensional formula of pressure to accurately obtain the axial thrust coefficient acting on the impeller. To unify the evaluation criteria, the value range of the legend is exactly identical under each operating condition. Therefore, although the axial thrust coefficient values exhibit obvious changes at different rotational speeds, no major differences in terms of the pressure coefficient are observed in the shroud cavity or rear cavity, due to the identical value range of the legend. More detailed analysis will be conducted in follow-up studies.

Corresponding to Figures 10 and 11, the same vertical section used in Figure 12 is utilized to obtain the distribution of the pressure coefficient. Select liquid oxygen as the simulation medium, Figure 13 shows the distribution of the static pressure with and without considering the thermodynamic effects.

As depicted in Figure 13, the pressure coefficient shows a slight reduction when the thermodynamic effects are considered, as shown in the red dotted ellipse. This can be interpreted in Figure 11 as the power loss leading to various physical properties, owing to the influence of thermodynamic effects. First, the pressure distributions in Figures 13(a)–13(c) are obtained under the premise of keeping the physical properties constant. In comparison of Figures 13(a)–13(c)

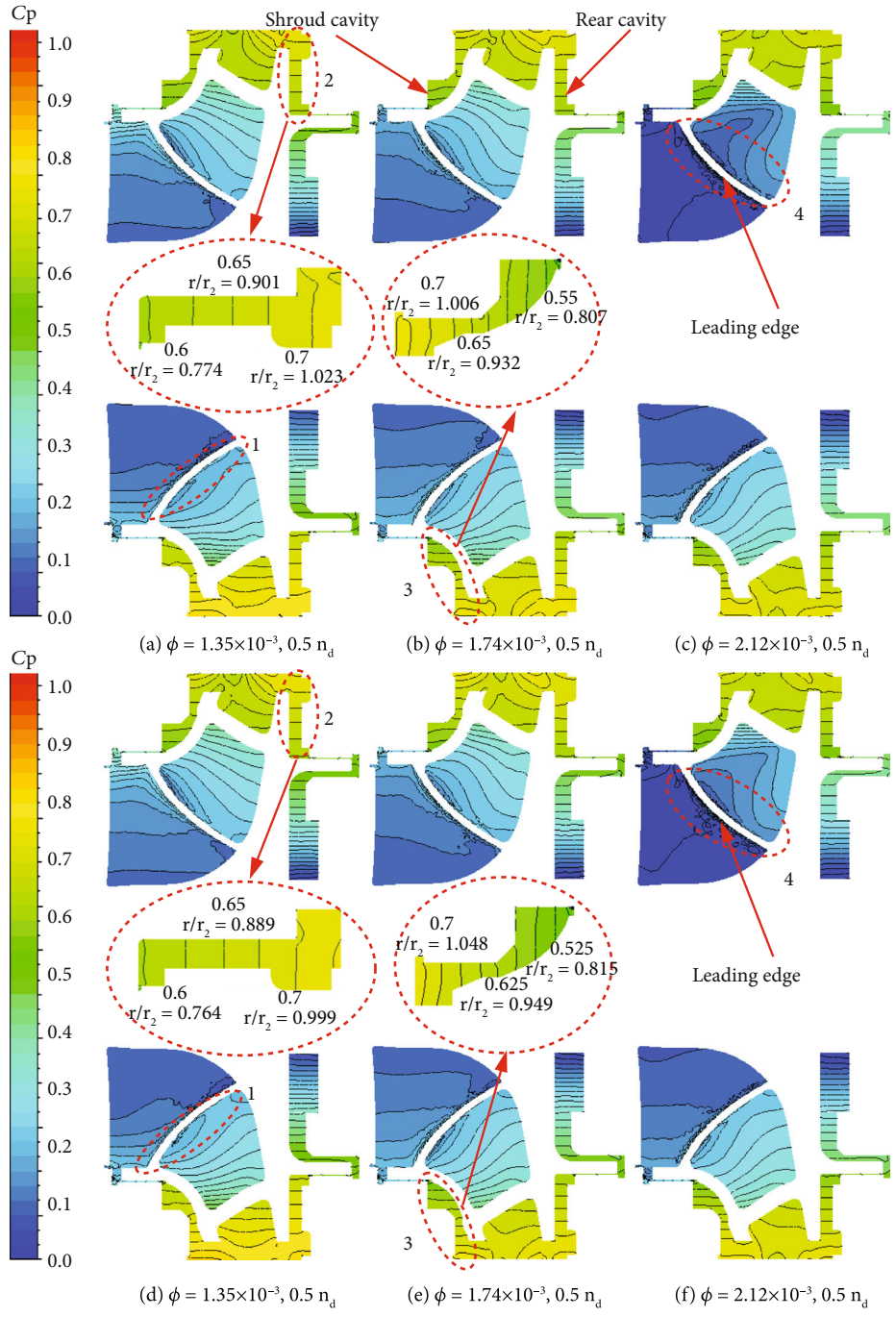

Figure 12: Comparison of the pressure field under different rotational speeds.

with Figures 12(a)–12(c), it clearly shows that the variations of the pressure coefficient under the same flow coefficient are almost identical. Regardless of whether the medium is water or liquid oxygen, the results show that the changes of the media do not affect the flow field distributions, just the divergences of the specific values occur because of the influence of the physical properties, which can be validated in Figure 10. As shown in Figures 13(a)–13(f), after considering the thermodynamic effects of liquid oxygen, the pressure coefficients in the main flow decrease at all flow coefficients, which can be clearly observed by comparing the pressure coefficient contours. Similar to the definition of head coefficient in Figure 10, the pressure coefficient values shown in Figures 13(d)–13(f) are obtained by using the density at the inlet boundary of the turbopump, which ignores the changes of local density caused by the thermodynamic effects. Therefore, this variable essentially expresses the pressure difference.

Similar with the pressure distributions in Figure 12, the static pressure in the main flow region gradually increases from the impeller eye to impeller outlet, where maximum static pressure zones appear near the impeller outlet.

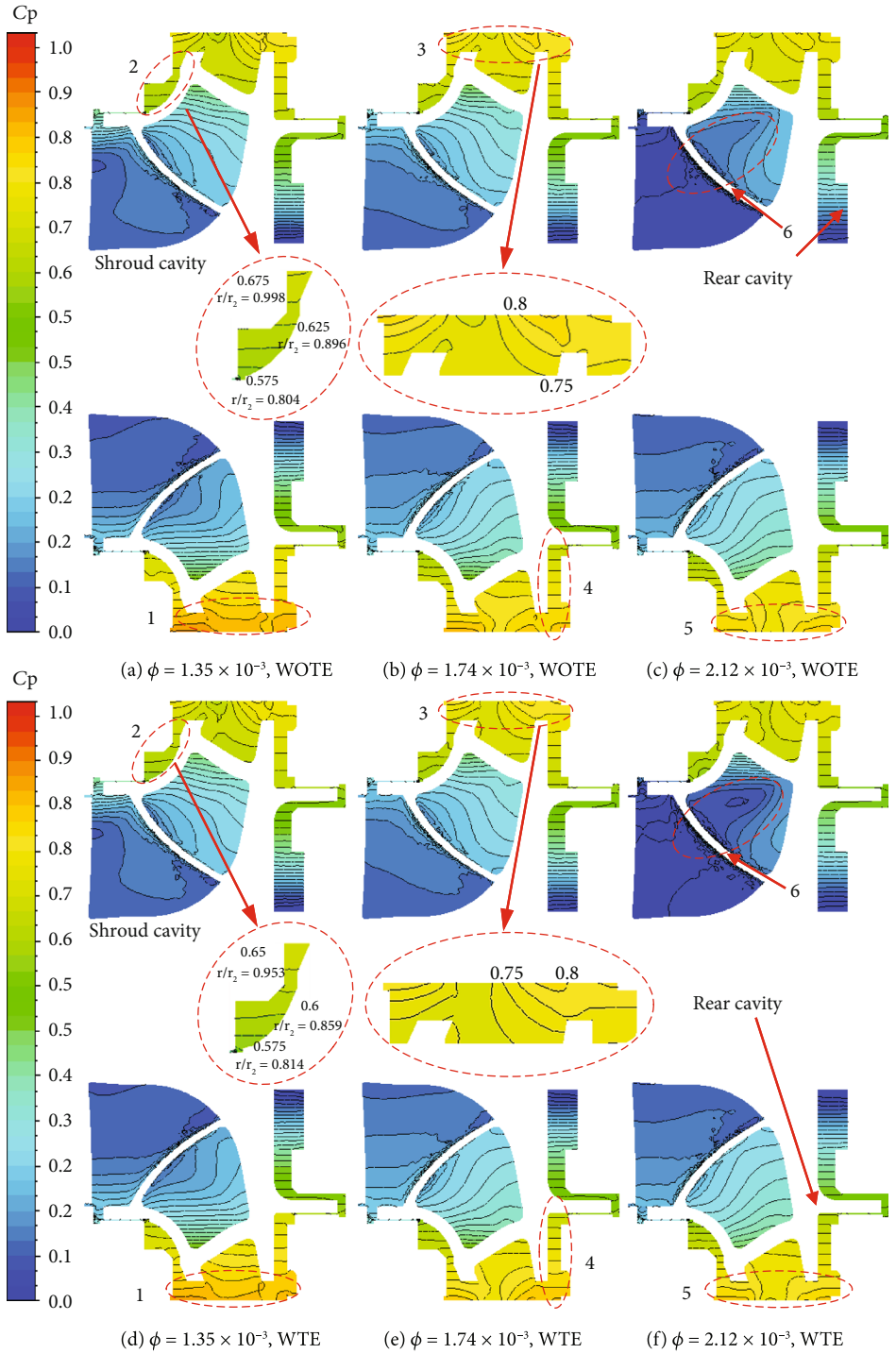

Figure 13: Comparison of the pressure field with and without thermodynamic effects.

Moreover, due to the rotor-stator interaction between the high-speed rotating impeller and the stationary volute, the static pressure distribution within the volute presents an obvious asymmetry along the circumferential direction. Comparative analysis of the pressure coefficient distributions in Figures 13(b) and 13(e) shows that the pressure coefficient values vary little at the inlet edge position of the impeller. However, as the medium is pressurized and conveyed downstream of the impeller, the difference of pressure coefficient between the two contours becomes more apparent, and more obvious differences of polylines. This feature is in accordance with the head coefficient simulated in Figure 10, which also can be observed in higher and lower flow coefficients. Fortunately, the characteristics of the static pressure in rotor-stator cavities still remain the same, which provides convenience for accurately solving the axial thrust after considering the thermodynamic effects. However, the divergences of the cavity pressure coefficient in Figure 13

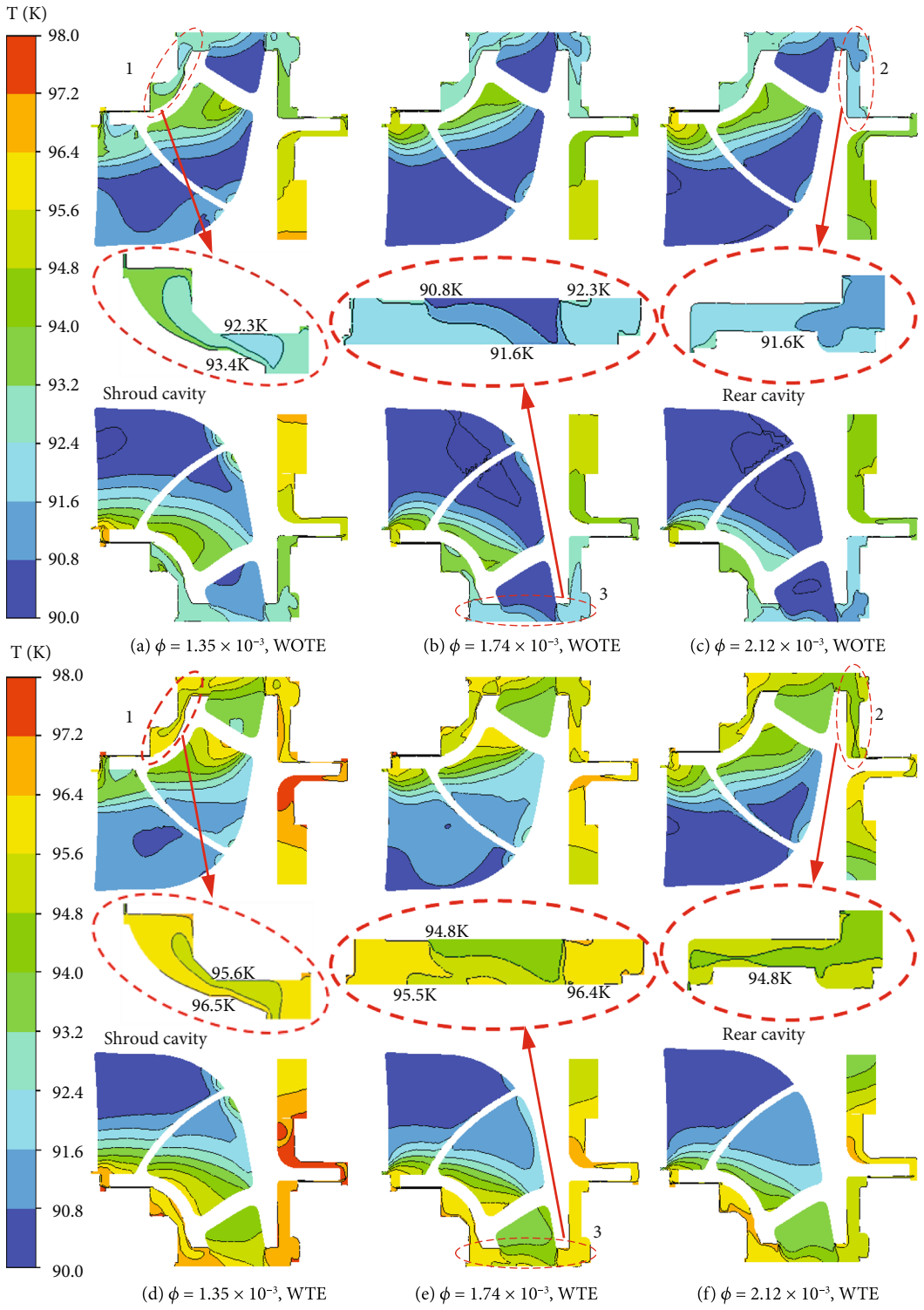

Figure 14: Comparison of the temperature with and without thermodynamic effects.

are obvious with those distributions in Figure 12, which are corresponding to the axial thrusts in Figures 9(a) and 11(b).

Owing to the thermodynamic effects of liquid oxygen, the distributions of pressure shown in Figure 13 are caused by the differences of the physical properties, which is essentially the variations of the temperature distribution, as shown in Figure 14. Whether the thermodynamic effects are considered or not, the temperature distributions in the rotational domains of the turbopump are closely related to the flowrate, which can be explained by the turbopump efficiency curve. Due to the influence of the rotor-stator cavity structure, the local temperature values in both the shroud cavity and the rear cavity are obviously higher than the main flow region. After considering the thermodynamic effects of

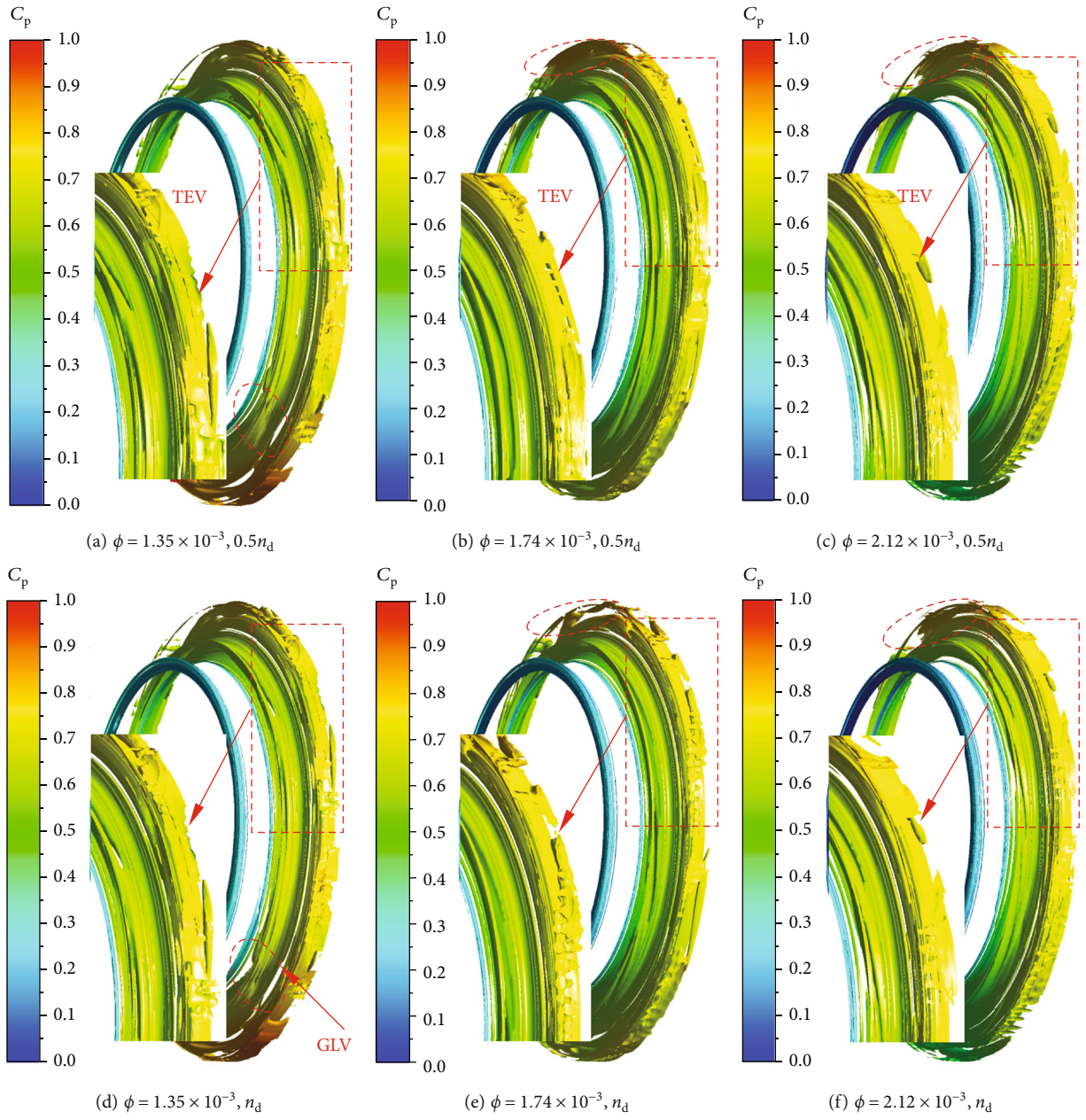

Figure 15: Comparison of the vortex under different rotational speeds.

liquid oxygen, the characteristics of the temperature distribution have not changed under all operating conditions, but the local corresponding values have increased significantly, especially at the impeller outlet and the rotor-stator cavities, as shown in Figures 14(a) and 14(d). The differences of the local temperature result in the variations of the physical properties of liquid oxygen. Finally, the turbopump head coefficients, efficiencies, and the axial thrusts in Figure 11 will be changed measurably, due to the consideration of thermodynamic effects.

4.4. Vortex Structures in Shroud Cavity. Vortex is a typical flow structure in fluid machineries and plays an important role in determining the overall performance of hydraulic machineries [54]. To investigate the vertical structures, the Q-criterion is applied to extract and obtain the vortex core region within the shroud cavity, which is widely used to determine complex flow structures. The Q-criterion can be described as follows:

$$Q = \frac{1}{2}\left(|\mathbf{\Omega}|^2 - |\mathbf{S}|^2\right), \tag{16}$$

with

$$\mathbf{\Omega} = \frac{1}{2}\left[\nabla \mathbf{v} - (\nabla \mathbf{v})^T\right]; \mathbf{S} = \frac{1}{2}\left[\nabla \mathbf{v} + (\nabla \mathbf{v})^T\right]. \tag{17}$$

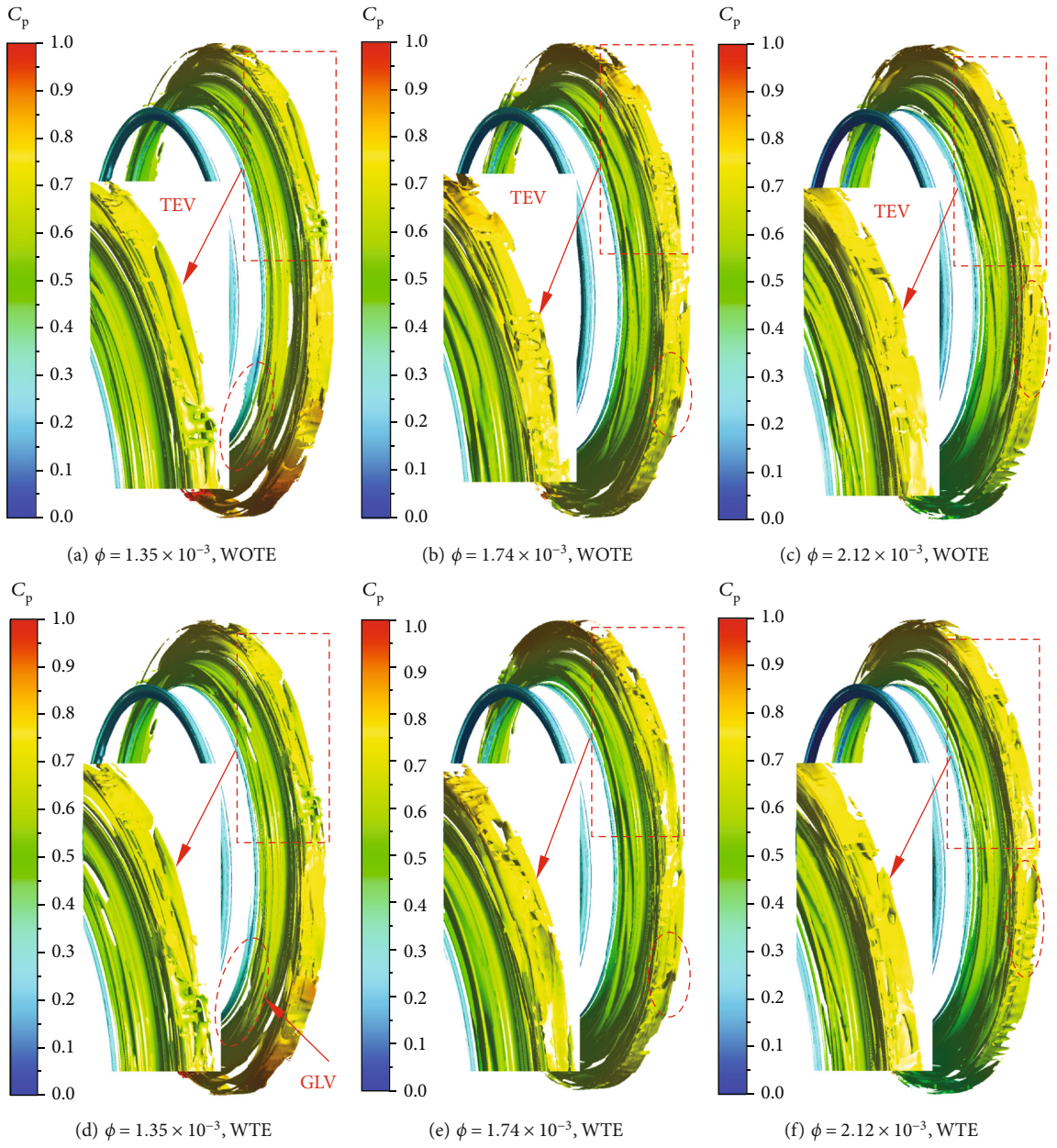

(a) $\phi = 1.35 \times 10^{-3}$, WOTE (b) $\phi = 1.74 \times 10^{-3}$, WOTE (c) $\phi = 2.12 \times 10^{-3}$, WOTE

(d) $\phi = 1.35 \times 10^{-3}$, WTE (e) $\phi = 1.74 \times 10^{-3}$, WTE (f) $\phi = 2.12 \times 10^{-3}$, WTE

Figure 16: Comparison of the vortex with and without thermodynamic effects.

Here, $\mathbf{\Omega}$ is the rotation rate tensor, and $\mathbf{S}$ is the strain rate tensor.

If $Q > 0$, the rotating force overcomes the strain force, and the rotating force maintains the predominant role. Furthermore, a large Q value indicates a large difference between the internal vorticity and the deformation rate.

For convenience of comparison, a nondimensional value of Q is usually employed, and the expression of Q^* is as follows:

$$Q^* > \sqrt{\frac{Q}{Q_{\max}}}. \tag{18}$$

Here, $Q_{\max}$ denotes to the maximum value of Q, which is extracted to determine the vortex core position in the vortex region identified by the Q-criterion.

To comprehensively characterize the three-dimensional vortex structures, the shroud cavity was selected as the research domain to analyze the influence of rotational speeds and thermodynamic effects. Figure 15 presents the vortices identified by Q-criterion at the rated and off-design conditions; the corresponding value is set as $Q^* = 0.006$ [55]. From Figure 15, some typical and significant vertical structures are captured by the Q-criterion.

As shown in Figure 15, the gap leakage vortex (GLV) is generated in the inlet domain. As the flow coefficient increases, the distribution and intensity of GLV correspondingly decrease. However, as the rotational speed decreases,

GLV exhibits opposite characteristics. A vortex structure is generated due to the rotor-stator interaction between the impeller and volute, pressure difference between the pressure and suction surface of the blade, and the momentum exchange between the main flow and secondary leakage flow. The main vortex generating area comprises three parts: the inlet, the cavity, and discharge domains (Figure 15(a)). The vortex in the inlet domain is mainly affected by the momentum exchange between the main and the leakage flows. The vortex structure in the cavity and discharge domains is controlled by the structures and the upstream boundary conditions.

Due to the impact of the rotor-stator interaction and leakage flow, the trailing edge vortex (TEV) and GLV can be observed at the inlet domain of the shroud cavity. Comparison of the vortex structure at different flow coefficients clearly shows that the size and strength of the vortex in the inlet domain negatively correlated with the flow coefficient, regardless of the rotational speed variation. In other words, the volume and strength of TEV and GLV in the inlet domain reaches the maximum at the small flow coefficient of $\phi = 1.35 \times 10^{-3}$. Due to the impact of the small clearance structure and leakage flow, the shroud cavity is almost filled with vortices, and the GLV volume in the cavity domain varies little within the simulated flow range, which can be seen from Figures 15(a) and 15(c). However, when the rotational speeds are varied and the flow coefficient are kept constant, the vortex structure in inlet domain significantly changes, as shown in Figures 15(b) and 15(e).

The vortex structures in Figures 15(d)–15(f) and Figures 16(a)–16(c) are clearly different. When the pressurized medium is changed from water to liquid oxygen, the dynamic viscosity of liquid oxygen is remarkably lower than that of water, which causes vortex breakdown at high flow rates or low operating conditions. Subsequently, to further analyze the influence of the thermodynamic effects, a comparison is performed on the vortex distribution considering the thermodynamic effects in the shroud cavity, as shown in Figures 16(d)–16(f). The dynamic viscosity of liquid oxygen is directly related to temperature. Turbulent dissipation leads to the temperature increase, leading to vortex separation at each flow coefficient. The volume of the vortex decreases when the influence of thermodynamic effects is considered which can be observed in Figures 16(b) and 16(e). These results correspond to the axial thrust coefficient in Figure 11(b) and reveal how the thermodynamic effects affect the distribution of the flow field in a cryogenic turbopump.

5. Conclusions

This paper is aimed at investigating the influence of rotational speeds and thermodynamic effects on the performance of a LOX turbopump. The accuracy of the numerical model was verified by comparing the head coefficients and efficiencies with the experimental data. The effects of rotational speeds and thermodynamic effects on the head coefficients, the efficiencies, and the axial thrusts acting on the impeller were analyzed in detail.

Taking water as the conveying medium, the numerical results reveal that the turbopump rotational speeds exhibit obvious effects on the efficiencies and axial thrusts. Under both normal condition and off-design conditions, as the rotational speed decreases, the total efficiencies gradually decrease and the head coefficients barely change. When the rotational speed of the turbopump increases from 0.5 n_d to n_d, the efficiencies via numerical simulated change from 72.5% to 73.8% at rated flow, which are very sensitive and essential for adjusting the parameters of the engine system. Unlike the external performance of the turbopump, the axial thrusts acting on either the impeller shroud or impeller hub monotonically increase, owing to the decrease of the rotational speeds. As the turbopump speed increases from $0.5n_d$ to n_d, the relative changes of the axial thrust acting on the impeller shroud and the impeller hub are 21.2% and 19.9% at rated flow, respectively. The affinity laws of the centrifugal pump can be used for quickly obtaining the head coefficients and efficiencies, but they are not suitable for obtaining the axial thrusts acting on the impeller.

Moreover, the influence of the thermodynamic effects on the abovementioned performance indicators was investigated. First, the thermodynamic effects of liquid oxygen and water were not considered; the head coefficients and efficiencies moderately change under all flow coefficients, due to the impact of dynamic viscosity. After taking into account the thermodynamic effects of liquid oxygen, the head coefficients and efficiencies significantly change, and the influencing trends are different obviously to the rotational speeds. The maximum relative variation of the head coefficient is 5.9% at $\phi = 2.12 \times 10^{-3}$, and that of efficiency is 4.3% under the same flow coefficient. The axial thrusts decrease by varying degrees, the deviation of 2.4% and 2.8% can be observed within the flow range. Due to the increase of temperature in the rotor-stator cavities, the axial thrust coefficients decrease with the magnitudes variation in the flow range. Therefore, the thermodynamic effects of liquid oxygen need to be considered for obtaining accurate axial thrust. Comparison of the internal flow and vortex shows that the rotational speeds and thermodynamic effects have significant impacts on the turbopump rotor-stator flow, which cannot be ignored for obtaining accurate turbopump performance.

The above results not only provide a deep understanding about the influence of rotational speeds and thermodynamic effects on the turbopump performance, but also some basic theoretical guidance for designers to determine the correct method. Based on the current results, further studies will be conducted to investigate the influence of thermodynamic effects on unsteady flow. Additionally, vortex analysis will be performed to further reveal the inner flow based on the incorporation of some advanced vortex identification methods.

Abbreviations

LOX: Liquid oxygen
LCH4: Liquid CH4

WTE: With thermodynamic effects
WOTE: Without thermodynamic effects
GLV: Gap leakage vortex
TEV: Trailing edge vortex.

Nomenclature

b: Axial width, mm
c_p: Specific heat capacity, kJ/kg.K
C_F: Axial thrust coefficient
C_{Fs}: Axial thrust coefficient acting on impeller shroud
C_{Fh}: Axial thrust coefficient on impeller hub
C_p: Pressure coefficient
D: Diameter, mm
H: Head, m
n: Rotational speed of the impeller, r/min
n_s: Specific speed
p: Static pressure, Pa
p_i: Inlet pressure of the turbopump, Pa
p_l: Local pressure, Pa
Q: Value from Q-criterion
Q^*: Nondimensional value of Q
Q_v: Volumetric flow rate, m^3/s
r: Radius, m
T: Temperature, K
T_p: Axial thrust, N
u: Circumferential velocity of a component, m/s
y^+: Y plus
Z: Number of impeller or inducer
$\mathbf{S}$: Strain rate tensor
$\nabla\mathbf{v}$: Velocity gradient tensor
ΔP: Pressure difference, Pa.

Greek Symbols

$\mathbf{\Omega}$: Rotation rate tensor
ϕ: Flow coefficient
ψ: Head coefficient
ρ: Density, kg/m^3
ω: Angular velocity of a rotating component, rad/s
λ: Thermal conductivity, W/m.K
μ: Dynamic viscosity, Pa.s.

Subscripts

d: Rated design condition
1: Inlet of a component
2: Outlet of a component
im: Impeller
in: Inducer.

Data Availability

The data used to support the findings of this study are included within the article.

Conflicts of Interest

The authors declare that they have no conflicts of interest.

Acknowledgments

This work is supported by the Distinguished Young Scholars of the National Natural Science Foundation of China (grant no. 51922085).

References

[1] G. P. Sutton, *Rocket Propulsion Elements*, John Willey&Sons, Inc, New Jersey, 9th edition, 2017.

[2] G. P. Sutton, "History of liquid-propellant rocket Engines in Russia, formerly the Soviet Union," *Journal of Propulsion and Power*, vol. 19, no. 6, pp. 1008–1037, 2003.

[3] G. P. Sutton, "History of liquid-propellant rocket engines in the United States," *Journal of Propulsion and Power*, vol. 19, no. 6, pp. 978–1007, 2003.

[4] R. F. Abdo, H. T. Pedro, R. N. Koury, L. Machado, C. F. Coimbra, and M. P. Porto, "Performance evaluation of various cryogenic energy storage systems," *Energy*, vol. 90, no. 1, pp. 1024–1032, 2015.

[5] Y. Ito, "The world's first test facility that enables the experimental visualization of cavitation on a rotating inducer in both cryogenic and ordinary fluids," *Journal of Fluids Engineering*, vol. 143, no. 12, article 121105, 2021.

[6] B. Nguyen, K. Faruqui, L. R. Robles et al., "Overview of current hybrid propulsion research and development," in *Proceedings of the ASME 2017 International Mechanical Engineering Congress and Exposition*, Florida, USA, November 2017.

[7] T. Kimura, T. Hashimoto, M. Sato et al., "Reusable rocket engine: firing tests and lifetime analysis of combustion chamber," *Journal of Propulsion and Power*, vol. 32, no. 5, pp. 1087–1094, 2016.

[8] S. R. Sargent, J. L. Preuss, and R. Pulling, "Low cost turbopump concept for wide throttle range applications," in *50th AIAA/ASME/SAE/ASEE Joint Propulsion Conference*, Cleveland, OH, July 2014.

[9] J. F. Gülich, *Centrifugal Pumps*, Springer-Verlag, Inc, Berlin, fourth edition, 2020.

[10] Y. Ogawa, N. Azuma, K. Aoki, T. Kobayashi, and K. Okita, "The Latest Development Status of LE-9 Engine Turbopumps," in *AIAA Propulsion and Energy Forum, AIAA 2018-4550*, Cincinnati, Ohio, July 2018.

[11] A. Apollonio, A. Anderlini, D. Valentini et al., "Concurrent theoretical, experimental and numerical analyses of mixed-flow turbopump design," *Aerospace Science and Technology*, vol. 123, article 107459, 2022.

[12] S. Martin, N. D. Jean-Michel, and P. Fonteyn, "Stability of hydrogen turbopump rotor shaft axially self-balanced," *Journal of Fluids Engineering*, vol. 144, no. 9, article 091206, 2022.

[13] Y. Tanaka, T. Kitabata, K. Nasu, S. Watanabe, and A. Sakata, "Suppression of cavitation surge in turbopump with inducer by reduced-diameter suction pipe with swirl brake," *Journal of Fluids Engineering*, vol. 144, no. 7, article 071205, 2022.

[14] C. H. Choi, J. G. Noh, D. J. Dae-Jin, S. S. Hong, and J. J. Kim, "Effects of floating-ring seal clearance on the pump performance for turbopumps," *Journal of Propulsion and Power*, vol. 25, no. 1, pp. 191–195, 2009.

[15] Y. Yang, L. Zhou, W. D. Shi, W. Li, and R. Agarwal, "Effect of rotating speed on performance of electrical submersible pump," in *8th Joint Fluids Engineering Conference*, San Francisco, CA, USA, July 2019.

[16] R. Xu, Y. Long, and D. Z. Wang, "Effects of rotating speed on the unsteady pressure pulsation of reactor coolant pumps with steam-generator simulator," *Nuclear Engineering and Design*, vol. 333, pp. 25–44, 2018.

[17] Y. D. Han and L. Tan, "Influence of rotating speed on tip leakage vortex in a mixed flow pump as turbine at pump mode," *Renewable Energy*, vol. 162, pp. 144–150, 2020.

[18] L. Dodsworth and D. Groulx, "Operational parametric study of a tesla pump: disk pack spacing and rotational speed," in *Proceedings of the ASME-JSME-KSME 2015 Joint fluids engineering conference*, Seoul, Korea, July 2015.

[19] H. Tsukamoto, H. Yoneda, and K. Sagara, "The response of a centrifugal pump to fluctuating rotational speed," *Journal of Fluids Engineering*, vol. 117, no. 3, pp. 479–484, 1995.

[20] E. M. A. Vermunt, K. A. J. Bruurs, M. S. Schoot, and B. P. M. Esch, "Part load instability and rotating stall in a multistage low specific speed pump," in *Proceedings of the ASME 2020 Fluids Engineering Division Summer Meeting, p.FEDSM 2020-20086, Intercontinental Toronto Centre*, Toronto, Ontario, Canada, July 2020.

[21] S. Ogata, A. Kimura, and K. Watanabe, "Effect of surfactant additives on centrifugal pump performance," *Journal of Fluids Engineering*, vol. 128, no. 4, pp. 794–798, 2006.

[22] X. H. Zheng, Y. N. Zhang, J. W. Li, and Y. N. Zhang, "Influences of rotational speed variations on the flow-induced vibrational performance of a prototype reversible pump turbine in spin-no-load mode," *Journal of Fluids Engineering*, vol. 142, no. 1, article 011106, 2020.

[23] R. J. Andrade-Cedeno, J. A. Pérez-Rodríguez, C. D. Amaya-Jaramillo, C. G. Rodríguez-Borges, Y. E. Llosas-Albuerne, and J. D. Barros-Enríquez, "Numerical study of constant pressure systems with variable speed electric pumps," *Energies*, vol. 15, no. 5, p. 1918, 2022.

[24] A. S. Kalaiselvana, U. Subramaniam, P. Shanmugam, and N. Hanigovszkic, "A comprehensive review on energy efficiency enhancement initiatives in centrifugal pumping system," *Applied Energy*, vol. 181, pp. 495–513, 2016.

[25] S. Oshurbekov, V. Kazakbaev, V. Prakht, V. Dmitrievskii, and L. Gevorkov, "Energy consumption comparison of a single variable speed pump and a system of two pumps: variable-speed and fixed-speed," *Applied Science*, vol. 10, no. 24, p. 8820, 2020.

[26] T. Tanaka and M. Tabaru, "Transient characteristics of a centrifugal pump at rapid startup," in *8th Joint Fluids Engineering Conference*, San Francisco, USA, July 2019.

[27] S. Duplaa, O. Coutier-Delgosha, A. Dazin, O. Roussette, G. Bois, and G. Caignaert, "Experimental study of a cavitating centrifugal pump during fast startups," *Journal of Fluids Engineering*, vol. 132, no. 2, article 021301, 2010.

[28] S. Duplaa, O. Coutier-Delgosha, A. Dazin, and G. Bois, "X-ray measurements in a cavitating centrifugal pump during fast start-ups," *Journal of Fluids Engineering*, vol. 135, no. 4, article 041204, 2013.

[29] F. Y. Jin, Z. F. Yao, D. M. Li, R. F. Xiao, F. J. Wang, and C. He, "Experimental investigation of transient characteristics of a double suction centrifugal pump system during starting period," *Energies*, vol. 12, no. 21, p. 4135, 2019.

[30] S. Watanabe, T. Hidaka, H. Horiguchi, A. Furukawa, and Y. Tsujimoto, "Analysis of thermodynamic effects on cavitation instabilities," *Journal of Fluids Engineering*, vol. 129, no. 9, pp. 1123–1130, 2007.

[31] S. Watanabe, T. Hidaka, H. Horiguchi, A. Furukawa, and Y. Tsujimoto, "Steady analysis of the thermodynamic effect of partial cavitation using the singularity method," *Journal of Fluids Engineering*, vol. 129, no. 2, pp. 121–127, 2007.

[32] K. Kikuta, Y. Yoshida, M. Watanabe, Y. Hashimoto, K. Nagaura, and K. Ohira, "Thermodynamic effect on cavitation performances and cavitation instabilities in an inducer," *Journal of Fluids Engineering*, vol. 130, no. 11, p. 11302, 2008.

[33] Y. Yoshida, Y. Sasao, M. Watanabe, T. Hashimoto, Y. Iga, and T. Ikohagi, "Thermodynamic effect on rotating cavitation in an inducer," *Journal of Fluids Engineering*, vol. 131, no. 9, article 091302, 2009.

[34] Y. Yoshida, H. Nanri, K. Kikuta, Y. Kazami, Y. Iga, and T. Ikohagi, "Thermodynamic effect on subsynchronous rotating cavitation and surge mode oscillation in a space inducer," *Journal of Fluids Engineering*, vol. 133, no. 6, article 061301, 2011.

[35] T. Tanaka, "Thermodynamic effect and cavitation performance of a cavitating centrifugal pump," in *Proceedings of the ASME-JSME-KSME 2011 Joint fluids engineering conference*, Hamamatsu, Shizuoka, Japan, July 2011.

[36] K. Kawatsu, N. Tani, and N. Yamanishi, "Influence of thermodynamic effect on cavitation suction performance of rocket engine inducer," in *51st AIAA Aerospace Sciences Meeting including the New Horizons Forum and Aerospace Exposition*, Grapevine, Texas, January 2013.

[37] J. Kim and S. J. Song, "Measurement of temperature effects on cavitation in a turbopump inducer," *Journal of Fluids Engineering*, vol. 138, no. 1, article 011304, 2016.

[38] D. J. Kim, H. J. Sung, C. H. Choi, and J. S. Kim, "Cavitation instabilities of an inducer in a cryogenic pump," *Acta Astronautica*, vol. 132, pp. 19–24, 2017.

[39] D. A. Ehrlich and J. W. Murdock, "A dimensionless scaling parameter for thermal effects on cavitation in turbopump inducers," *Journal of Fluids Engineering*, vol. 137, no. 4, article 041103, 2015.

[40] L. Xiang, H. Chen, Y. H. Tan, K. F. Xu, and J. N. Liu, "Study of thermodynamic cavitation effects in an inducer," *Journal of Propulsion and Power*, vol. 36, no. 3, pp. 312–322, 2020.

[41] D. Y. Li, Z. P. Ren, Y. Li, B. X. Miao, R. Z. Gong, and H. J. Wang, "Thermodynamic effects on pressure fluctuations of a liquid oxygen turbopump," *Journal of Fluids Engineering*, vol. 143, no. 11, article 111401, 2021.

[42] H. Negishi, S. Ohno, and M. Tsutomu, "Numerical analysis of unshroud impeller flowfield in the LE-X liquid hydrogen pump," in *53rd AIAA/SAE/ASEE Joint Propulsion Conference*, Atlanta, GA, July 2017.

[43] H. Kawashima, T. Kobayashi, and K. Okita, "Progress of LE-9 engine development," in *2018 Joint Propulsion Conference*, Cincinnati, Ohio, July 2018.

[44] N. Azuma, M. Kojima, T. Kobayashi, K. Okita, T. Motomura, and K. Niiyama, "The development status of LE-9 engine turbopumps for H3 launch vehicle," in *AIAA Propulsion and Energy 2019 Forum*, Indianapolis, IN, August 2019.

[45] X. B. Bu, H. C. Cong, Z. G. Sun, and G. Xi, "Influence of thermodynamic effects on rotor–stator cavity flow in liquid oxygen turbopump," *Physics of Fluids*, vol. 35, no. 2, article 0137980, 2023.

[46] D. S. Zhang, Q. Zhou, Q. Gu et al., "Experimental and numerical investigation on the transient cavitating flows in a mixed

flow pump with different number of blades at startup," *Journal of Fluids Engineering*, vol. 144, no. 5, article 051204, 2022.

[47] F. R. Menter, M. Kuntz, and R. Langtry, "Ten years of industrial experience with the SST turbulence model," *Turbulence, Heat and Mass Transfer*, vol. 4, pp. 625–632, 2003.

[48] L. Chabannes, D. Stefan, and P. Rudolf, "Effect of splitter blades on performances of a very low specific speed pump," *Energies*, vol. 14, no. 13, p. 3785, 2021.

[49] A. Patil and G. Morrison, "Affinity law modified to predict the pump head performance for different viscosities using the Morrison number," *Journal of Fluids Engineering*, vol. 141, no. 2, article 021203, 2019.

[50] K. Kamijo, H. Yamada, N. Sakazume, and S. Warashina, "Developmental history of liquid oxygen turbopumps for the LE-7 engine," *Transactions of the Japan Society for Aeronautical and Space Sciences*, vol. 44, no. 145, pp. 155–163, 2001.

[51] S. Maier, B. Wagner, L. Veggi, J. D. Pauw, and P. Beck, "Analytical and numerical assessment of axial thrust balancing systems in liquid rocket engine LOx turbopumps," in *7th European Conference for Aerospace Sciences*, Politecnico di Milano, Milan, Italy, 2017.

[52] *Reference Fluid Thermodynamic and Transport Properties Database V10.0, the National*, Institute of Standards and Technology, 2021.

[53] Y. S. Zeng, Z. F. Yao, F. J. Wang, R. F. Xiao, and C. L. He, "Experimental investigation on pressure fluctuation reduction in a double suction centrifugal pump: influence of impeller stagger and blade geometry," *Journal of Fluids Engineering*, vol. 142, no. 4, article 041202, 2020.

[54] Y. N. Zhang, K. H. Liu, H. Z. Xian, and X. Z. Du, "A review of methods for vortex identification in hydroturbines," *Renewable and Sustainable Energy Reviews*, vol. 81, no. 1, pp. 1269–1285, 2018.

[55] N. Zhang, J. X. Jiang, B. Gao, X. K. Liu, and D. Ni, "Numerical analysis of the vortical structure and its unsteady evolution of a centrifugal pump," *Renewable Energy*, vol. 155, pp. 748–760, 2020.